



UNIVERSIDAD DE INVESTIGACIÓN DE TECNOLOGÍA EXPERIMENTAL YACHAY

Escuela de Ciencias Físicas y Nanotecnología

TÍTULO: Study of the Photoconductance of TiO₂ and ZnO Semiconductors in a Chitosan Matrix

Trabajo de integración curricular presentado como requisito para
la obtención del título de Ingeniero en Nanotecnología

Autor:

Guaman Rivas Luis Alexander

Tutor:

Ph.D. – Bramer Werner

Co-tutora:

Ph.D. – González Gema

Urququí, Mayo del 2024

AUTORÍA

Yo, **GUAMAN RIVAS LUIS ALEXANDER**, con cédula de identidad 1104882830, declaro que las ideas, juicios, valoraciones, interpretaciones, consultas bibliográficas, definiciones y conceptualizaciones expuestas en el presente trabajo; así cómo, los procedimientos y herramientas utilizadas en la investigación, son de absoluta responsabilidad de el/la autor (a) del trabajo de integración curricular. Así mismo, me acojo a los reglamentos internos de la Universidad de Investigación de Tecnología Experimental Yachay.

Urcuquí, Mayo del 2024.

Luis Alexander Guaman Rivas
CI: 1104882830

AUTORIZACIÓN DE PUBLICACIÓN

Yo, **GUAMAN RIVAS LUIS ALEXANDER**, con cédula de identidad 1104882830, cedo a la Universidad de Investigación de Tecnología Experimental Yachay, los derechos de publicación de la presente obra, sin que deba haber un reconocimiento económico por este concepto. Declaro además que el texto del presente trabajo de titulación no podrá ser cedido a ninguna empresa editorial para su publicación u otros fines, sin contar previamente con la autorización escrita de la Universidad.

Asimismo, autorizo a la Universidad que realice la digitalización y publicación de este trabajo de integración curricular en el repositorio virtual, de conformidad a lo dispuesto en el Art. 144 de la Ley Orgánica de Educación Superior

Urcuquí, Mayo del 2024.

Luis Alexander Guaman Rivas
CI: 1104882830

Dedication

This work is dedicated to my beloved family, my mother, my father, my siblings and my grandmother, fundamental pillars in my life.

Luis Alexander Guaman Rivas

Acknowledgements

First, I would like to thank God for allowing me to live this beautiful stage of my life. I would also like to thank my mother Alexandra, who has been supporting me unceasingly throughout my life, my father Luis, my grandmother Isabel and my siblings Gustavo, Ingrid and Dayrita; everything I do, I do this for and because of them. A very special thanks to my tutor, Ph.D. Werner Bramer; I could not find better support than him in terms of knowledge, energy and perseverance. To my (co)tutor Ph.D. Gema Gonzalez who helped me in key aspects to achieve better results. A loving thank you to Fernanda, who made my days in Yachay not monotonous and my stay much more colorful and meaningful. I am grateful to many colleagues in this university. Christian, my very sincere and unconditional friend. Rojo, my great friend who was always there for me when I needed him. Jony, Pedro and Kevin, my friends of fun and conversation. Thank all my soccer friends, especially my team "Vendetta F.C.", my team that never gives up. I also want to give recognition to many great professors with whom I could cross, my dear professor MSc. Lola de Lima, Ph.D. Aracelis Hernandez, Ph.D. Sarah Briceño, Ph.D. Franklin Camacho, excellent people who have taught me a lot not only with scientific knowledge but also a lot of knowledge of life and not to give up. Many thanks to those who made this project possible, Josue, Ph.D. Jhony Chimborazo, MSc. Lola de Lima, and lab technicians Johana and Mafer.

Also, I want to make a special mention to my beloved pets, Gandhi, Hammed and Melo, who went to a better place during the course of my career, but every time I saw them, they cheered up my existence.

Luis Alexander Guaman Rivas

Resumen

Este estudio examina a fondo las características de fotoconductancia de nanopartículas semiconductoras de TiO_2 y ZnO cuando se incorporan a una matriz de quitosano para evaluar su idoneidad para usos optoelectrónicos ecológicos y no tóxicos. Este estudio pretende descubrir materiales alternativos que sean inertes y amigables con el medio ambiente en respuesta a las peligrosas consecuencias de los fotorresistores tradicionales que contienen sustancias químicas venenosas como el sulfuro de cadmio y el sulfuro de plomo. En este estudio se utilizaron películas de quitosano combinadas con una estructura interdigitada, incorporando cantidades variables de nanopartículas de TiO_2 y ZnO . Se utilizó quitosano de peso molecular medio, necesario y apropiado para el estudio. Se crearon nanopartículas de TiO_2 y nanopartículas de ZnO , se crearon interdigitados mediante un proceso minucioso y se diseñó un circuito específico para medir las muestras. El estudio explica cómo se creó un sistema especializado para probar la fotoconductancia, centrándose en cómo el tamaño y la dispersión de las nanopartículas afectan a la eficiencia de la fotoconductancia. El examen por DRX mostró el tamaño de los cristallitos y la pureza de las fases. Por el contrario, las mediciones DLS sugirieron un mayor tamaño de partícula causado por la aglomeración, resultado que se profundizó mediante imágenes AFM. Se utilizaron la espectroscopia UV-Vis y el análisis del gráfico de Tauc para identificar las energías de banda prohibida críticas para las propiedades fotoactivas del semiconductor.

El trabajo se centra en mejorar la producción de películas compuestas a base de quitosano abordando los problemas que surgen durante el proceso de secado y haciendo hincapié en la importancia de gestionar las condiciones de síntesis para evitar la degradación de la película. El estudio demuestra que, cuando se incorporan al quitosano, las nanopartículas de TiO_2 y ZnO presentan características fotoconductoras favorables. Sin embargo, la mejora es significativamente mayor con TiO_2 . Además, se observan comportamientos intrigantes con implicaciones potenciales para el desarrollo de dispositivos electrónicos más seguros y sostenibles. Los resultados se suman a la creciente comprensión de los compuestos semiconductores y subrayan la importancia de seleccionar los materiales adecuados para impulsar el progreso tecnológico en consonancia con la sostenibilidad medioambiental.

Palabras clave: Quitosano, dióxido de titanio, óxido de zinc, nanopartículas, películas, fotoconductancia.

Abstract

This study thoroughly examines the photoconductance characteristics of semiconducting TiO₂ and ZnO nanoparticles when incorporated into a chitosan matrix to assess their suitability for eco-friendly and non-toxic optoelectronic uses. This study aims to discover alternative materials that are inert and environmentally friendly in response to the dangerous consequences of traditional photoresistors containing poisonous chemicals like cadmium sulfide and lead sulfide. This study utilized chitosan films combined with an interdigitated structure, incorporating varying quantities of TiO₂ and ZnO nanoparticles. Medium molecular weight chitosan was utilized, which was necessary and appropriate for the study. TiO₂ nanoparticles and ZnO nanoparticles were created, interdigitates were made by a thorough process, and a specific circuit was designed to measure the samples. The thesis explains how a specialized system was created to test photoconductance, focusing on how nanoparticle size and dispersion affect photoconductance efficiency. XRD examination showed the size of crystallites and the purity of phases. In contrast, DLS measurements suggested greater particle size caused by agglomeration, a result that was elaborated on by AFM imaging. UV-Vis spectroscopy and Tauc diagram analysis were used to identify the critical bandgap energies for the semiconductor's photoactive properties.

The work focuses on improving the production of chitosan-based composite films by addressing issues that arise during the drying process and emphasizing the significance of managing synthesis conditions to prevent film degradation. The study demonstrates that when incorporated into chitosan, TiO₂ and ZnO nanoparticles display favorable photoconductive characteristics. However, the improvement is significantly greater with TiO₂. Additionally, intriguing behaviors with potential implications for developing safer and more sustainable electronic devices are noted. The findings add to the increasing understanding of semiconductor composites and emphasize the significance of selecting appropriate materials to drive technological progress in alignment with environmental sustainability.

Keywords: Chitosan, titanium dioxide, zinc oxide, nanoparticles, films, photoconductance.

Contents

List of Figures	x
1 Introduction	1
1.1 Problem Statement	2
1.2 General and Specific Objectives	3
2 Theoretical Background	5
2.1 Semiconductor Nanoparticles	5
2.1.1 Intrinsic Semiconductors	6
2.1.2 Extrinsic Semiconductors	6
2.1.3 Binary nanoparticles	8
2.1.4 Binary metal oxides	8
2.2 Chitin and Chitosan (Ch): molecular structures	9
2.2.1 Source	9
2.2.2 Production of Chitosan	9
2.2.3 Biosynthesis of chitosan	10
2.2.4 Physical properties of Chitosan	11
2.2.5 Biological Sources of Composition:	12
2.3 Mott conduction	12
2.3.1 Chitosan/TiO ₂ Composite	14
2.3.2 Chitosan/ZnO Composite	15
3 Methodology	17
3.1 Reagents and Equipment	17
3.1.1 Equipment	17
3.1.2 Materials and chemicals	17
3.2 Fabrication of Interdigitates	18
3.3 Synthesis of TiO ₂ Nanoparticles	19

3.4	Synthesis of ZnO nanoparticles	20
3.5	Characterization Techniques	21
3.5.1	Ultraviolet-Visible-Near Infrared Spectroscopy (UV/Vis/NIR)	21
3.5.2	X-Ray Diffraction (XRD)	21
3.5.3	Dynamic Light Scattering (DLS)	21
3.5.4	Atomic Force Microscopy (AFM)	22
3.6	Dilution of Chitosan	22
3.7	Preparation of Ch/TiO ₂ solution	23
3.8	Preparation of Ch/ZnO solution	23
3.9	Preparation of Ch/TiO ₂ /ZnO solution	24
3.10	Film Fabrication on Interdigitated Electrodes:	24
3.11	Equipment for measurements	25
4	Results & Discussion	29
4.1	Interdigitates obtained and their scale	29
4.2	TiO ₂ nanoparticles obtained	30
4.3	ZnO nanoparticles obtained	31
4.4	UV-Vis Spectroscopy Characterization	32
4.5	Powder X-Ray Diffraction (XRD) Characterization	33
4.6	Dynamic Light Scattering (DLS) Characterization	36
4.7	Atomic Force Microscopy (AFM) Characterization	38
4.8	Sonication dispersion of nanoparticles in the chitosan solution	40
4.9	Films fabricated on interdigitated electrodes	42
4.10	Photoconductivity of Ch/TiO ₂ Composite Films	43
4.10.1	Effects of the assigned TiO ₂ concentrations	44
4.11	Photoconductivity of Ch/ZnO Composite Films	47
4.11.1	Effects of the assigned ZnO concentrations	47
4.12	Photoconductivity of Ch/TiO ₂ /ZnO Composite films	49
4.12.1	Effects of the assigned TiO ₂ /ZnO concentrations	49
4.13	General Discussion	51
5	Conclusions & Outlook	53
5.1	Future research	54
A	Short Appendix 1 Heading for the Table of Contents	55
	Bibliography	57

List of Figures

1.1	Schematic representation of hybrid composite preparation: (a) mechanical stirring, (b) coatingsurface, and (c) nanocomposite. ⁵	2
2.1	Different solid materials with their respective Band gaps. ⁹	5
2.2	Intrinsic Semiconductor's Energy Band Diagram at (a) 0k and (b) Temperature > 0k. ¹¹	6
2.3	Classes of wide bandgap semiconductor materials shown in a schematic network diagram. A group of anions is used to classify the classes. ¹⁴	7
2.4	Steps to extract Shrimp chitosan. ²⁶	10
2.5	Structures of cellulose and chitin. ²⁵	11
3.1	Graphical scheme of the steps to follow for fabrication of interdigitatedes.	18
3.2	Graphical scheme of the steps to follow for TiO ₂ synthesis.	19
3.3	Chemical reactions occurring in each process of the synthesis. ⁵⁵	20
3.4	Graphical scheme of the steps to follow for ZnO synthesis.	20
3.5	Representation for the process of the films, A) the materials required, B) drop-by-drop films before sun drying, and C) the measurement of each of the composites.	25
3.6	Graphical representation of the circuit used created in "Proteus" to verify its operation.	25
3.7	Homemade measuring equipment, A) connection of the electrodes to the interdigitate seen from above, B) base created including the UV source seen from the front, C) external circuit with its modifiable resistance, D) DAQ system.	27
3.8	Scheme of the steps to follow for the realization of each one of the solutions, taking into account the respective changes in each one.	28
4.1	Interdigitated developed with respective reference measurements, the height, the width and the electrode spacing.	29
4.2	Results of the TiO ₂ nanoparticles synthesis with A) The solution obtained from the synthesis and B) the TiO ₂ powder obtained after the calcination process.	30
4.3	Results of the ZnO nanoparticles synthesis with A) The solution obtained from the synthesis and B) the ZnO powder obtained after the calcination process.	31

4.4	Optical Reflectance (%R) obtained of TiO ₂ and ZnO NPs.	32
4.5	Tauc plot obtained to find the band gap of TiO ₂ and ZnO NPs.	33
4.6	XRD pattern of TiO ₂ nanoparticles.	34
4.7	XRD pattern of ZnO nanoparticles.	35
4.8	DLS measurement to determine the size distribution of TiO ₂ NPs in the chitosan matrix.	36
4.9	DLS measurement to determine the size distribution of ZnO NPs in the chitosan matrix.	37
4.10	AFM analysis images for the morphology of Ch/TiO ₂ . The normal and the 3D image by applying lightning color.	38
4.11	AFM analysis images for the morphology of Ch/ZnO. The normal and the 3D image by applying overlay color.	39
4.12	AFM analysis images for the morphology of Ch/TiO ₂ /ZnO. The normal and the 3D image by applying lightning color.	40
4.13	Each of the solutions obtained after the sonication process. Each at 0.7% w/v.	41
4.14	Gelation of the Ch/ZnO solution by not adding 20% acetic acid.	41
4.15	Composite added to the interdigitate for the drying process, each one delimited. Ch/TiO ₂ , Ch/ZnO, Ch/TiO ₂ /ZnO respectively.	42
4.16	Films created after the drying stage. Ch/TiO ₂ , Ch/ZnO, Ch/TiO ₂ /ZnO respectively.	43
4.17	Rise and fall curves of Ch/TiO ₂ depending on exposure and non-exposure to UV light(all concentrations).	44
4.18	Rise and fall curves of Ch/TiO ₂ depending on exposure and non-exposure to UV light(0.01 and 0.1).	45
4.19	Rise and fall curves of Ch/TiO ₂ depending on exposure and non-exposure to UV light(0.5 and 0.7).	46
4.20	Rise and fall curves of Ch/ZnO depending on exposure and non-exposure to UV light(0.01 and 0.1).	47
4.21	Rise and fall curves of Ch/ZnO depending on exposure and non-exposure to UV light(0.5 and 0.7).	48
4.22	Rise and fall curves of Ch/TiO ₂ /ZnO depending on exposure to UV light(0.1 and 0.5).	49
4.23	Rise and fall curves of Ch/TiO ₂ /ZnO 0.7% depending on exposure to UV light.	50
A.1	Mean size of TiO ₂ nanoparticles with XRD data using the fundamental parameters of the equipment software at each of the highest peaks.	55
A.2	Mean size of ZnO nanoparticles with XRD data using the fundamental parameters of the equipment software at each of the highest peaks.	56

Chapter 1

Introduction

Research on nanomaterials has grown at an exponential rate in the modern era. Nanomaterials can have sizes ranging from 1 to 100 nm, and their dimensions can be reduced in one, two, or all three directions to create thin wires, dots, or films, respectively. Nanomaterials can also have a variety of shapes, and their size and/or shape can affect their qualities. These substances include semiconductors, metal oxides, organic compounds, biomaterials, or metals. As a result, there is a huge opportunity to create novel materials with interesting properties¹. A structure confined in all three dimensions (x, y, and z) is called a nanoparticle. On the other hand, a structure that exists in just two dimensions is shaped like a nanowire or nanorod. A thin film is confined to the z-direction even though it can extend across great distances in both the x and y axes. Particles are typically analyzed and characterized as spheres or rods, even though their crystal structure frequently results in complex morphologies².

Semiconductors have properties halfway between conductivity and insulativity. They are vital components of contemporary electronics, serving as the foundation for semiconductor devices, including integrated circuits, transistors, and diodes. Semiconductors are essential for controlling the flow of electrical current in electronic devices, which makes them essential for information manipulation and processing. By doping semiconductors with impurities, it is possible to alter their electrical conductivity, creating complex electronic components that sustain the contemporary digital world³.

Recently, there has been a significant rise in the immobilization of inorganic compounds onto organic supporting materials. This is primarily due to the advancement of hybrid composites, which are typically created by combining proteins, starch, gums, and chitosan with ZnO, Ag, CuO, and TiO₂ nanoparticles (NPs)⁴.

The most common method for preparing organic-inorganic hybrid-based composites involves mechanical stirring in Figure 1.1a, where a metal is mixed with a polymeric matrix, potentially forming chemical interactions. The technological properties of the composite depend on the mixing ratio of the polymer and metal oxide; the coating method in Figure 1.1b, where the metal oxide is deposited in the polymeric surface matrix by electrochemical and/or physical deposition; and the nanocomposite method in Figure 1.1c, where involves chemically bonding the polymer and metal oxide. Nonetheless, The metal oxide can serve as a crosslinking agent, enhancing the mechanical characteristics of polymeric and film-forming solutions⁵. The complete graphic representation is in Figure 1.1.

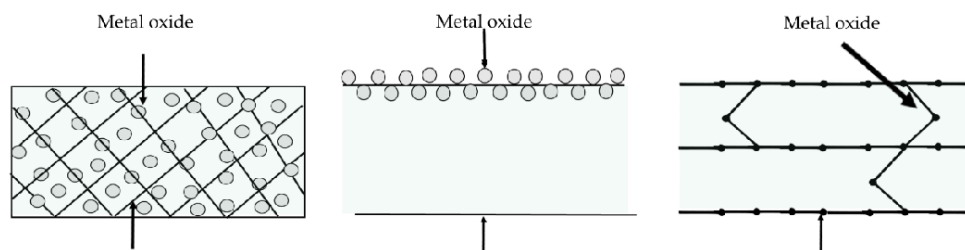


Figure 1.1: Schematic representation of hybrid composite preparation: (a) mechanical stirring, (b) coatings surface, and (c) nanocomposite.⁵

The study of semiconductor materials such as titanium dioxide (TiO_2) and zinc oxide (ZnO) has played a crucial role in advancing the areas of photocatalysis, solar energy conversion and environmental cleanup. These materials are renowned for their broad bandgap, high electronic mobility and outstanding stability when exposed to photoirradiation. The integration of these semiconductors into a biopolymer matrix, such as chitosan, offers a new method to improve their physical characteristics and photoconductivity. TiO_2 and ZnO are known for their high photocatalytic efficiency, essential for many applications, such as dye-sensitized solar cells (DSSCs) and environmental cleaning⁶. The qualities of ZnO compared to TiO_2 , such as electron mobility and stability, were highlighted, and it is positioned as a favorable choice for utilization. Likewise, ZnO/TiO_2 nanocomposites were studied to combine the unique characteristics of both semiconductors and to see if there is an improvement in their stability and photocatalytic efficiency⁷.

Chitosan, a natural biopolymer, provides a flexible structure to incorporate semiconducting nanoparticles, potentially improving charge separation, decreasing electron-hole recombination and boosting photocatalytic performance. Combining metal oxide semiconductors with chitosan is an effective method to reduce wastewater pollutants. The large surface area of chitosan and its adsorption properties make it an ideal material for wastewater treatment⁸.

Thus, this research covers the production of TiO_2 and ZnO nanoparticles in a chitosan matrix, the characterization of the compounds, and the creation of efficient measurement equipment for the evaluation of their photoconductance properties. This research aims to contribute to the development of new materials by explaining how the semiconducting nanoparticles interact with the chitosan matrix. These materials could have diverse applications in solar energy conversion, environmental remediation and other sectors. In the future, these findings could offer important prospects for creating advanced semiconductor materials for other technological uses.

1.1 Problem Statement

The widespread use of cadmium sulfide and lead sulfide in photoresistors across electronic devices poses a significant environmental and health hazard due to their toxicity and carcinogenic nature. Inadequate disposal of these substances leads to soil and water contamination, necessitating the exploration of safer, eco-friendly alternatives. Integrating TiO_2 and ZnO within a chitosan matrix offers a compelling solution, attributable to their non-toxic and biodegradable

nature and superior semiconducting properties.

1.2 General and Specific Objectives

General Objective

To investigate the photoconductance properties of TiO_2 and ZnO semiconductors within a chitosan matrix, focusing on their applications in optoelectronic devices.

Specific Objectives

- Synthesize ZnO (NPs) and TiO_2 (NPs)
- Synthesize composite films of TiO_2 (NPs)- ZnO (NPs) in the Chitosan matrix.
- Characterize the materials involved, including TiO_2 and ZnO and those in the Chitosan Matrix to provide a comprehensive understanding of their structural properties.
- Design and manufacture the appropriate interdigitates for effective measurement.
- Identify key factors influencing the formation of films on interdigitated substrates and the photoconductivity response of these (TiO_2 - ZnO -chitosan composite).
- Examine the impact of a chitosan matrix on the photoconductance properties of TiO_2 and ZnO .

Chapter 2

Theoretical Background

2.1 Semiconductor Nanoparticles

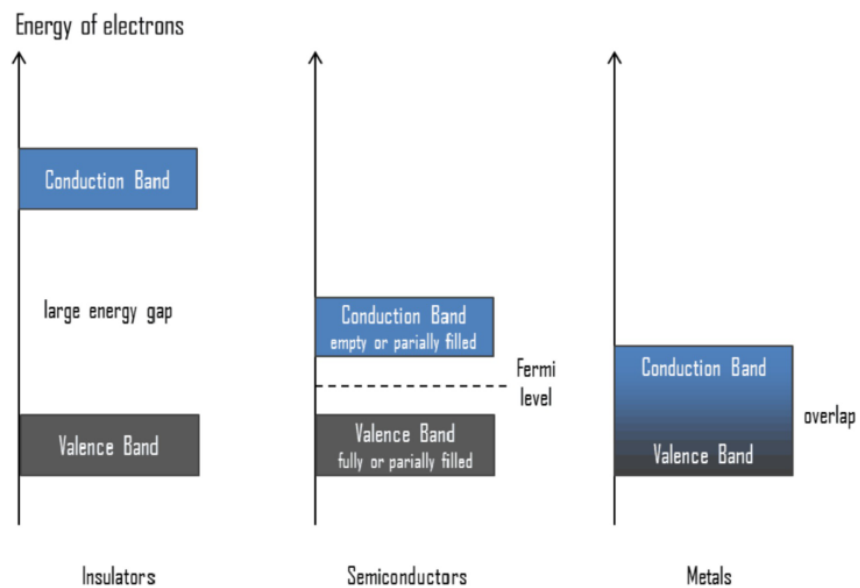


Figure 2.1: Different solid materials with their respective Band gaps.⁹

Visualizing the differences between conductors, insulators, and semiconductors can be achieved by plotting the available energies for the electrons in the various materials. The alternative energy states form bands instead of separate energies as in the case of unbound atoms. The existence of electrons in the conduction band is necessary for the conduction process to occur. In insulators, the valence band's electrons are separated from the conduction band

by a large gap; in conductors, like metals, the valence band overlaps the conduction band; and in semiconductors, the gap between the valence and conduction bands is small enough for thermal or other pulses to pass through. Semiconductors can be broadly categorized as intrinsic and extrinsic semiconductors⁹. Intrinsic semiconductors can potentially be referred to as pure or undoped elements. In contrast, extrinsic semiconductors are doped with other substances, sometimes called impurities, and they can be either n-type, defined as having mostly free electrons, or p-type, defined as having mostly free holes¹⁰.

2.1.1 Intrinsic Semiconductors

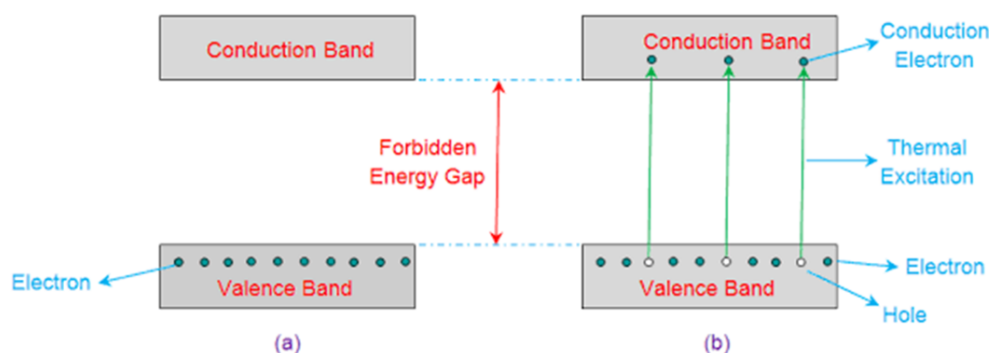


Figure 2.2: Intrinsic Semiconductor's Energy Band Diagram at (a) 0k and (b) Temperature > 0k.¹¹

The reagents to be used in this project both ZnO and TiO₂ are intrinsic semiconductors. As seen in Figure 2.2, an intrinsic semiconductor is a pure semiconductor material in which the number of holes in the conduction band equals the number of electrons¹¹. An additional distinguishing characteristic of an intrinsic semiconductor is that both are n-type intrinsic semiconductors; therefore, its Fermi level is located near the conduction band. Also regardless of being intrinsic, in these semiconductors, the forbidden energy gap is extremely small, and the valence electrons can move from room temperature energy to the conduction band with only that small amount of energy.

In the event of a potential difference applied across an intrinsic semiconductor, electrons will flow toward the positive terminal and holes will drift toward the negative terminal. Free electron and hole currents result in the total current flowing through a semiconductor. The number of hole-electron pairs and the current flowing through the semiconductor increase with semiconductor temperature. Put another way; it depends on the temperature⁹.

2.1.2 Extrinsic Semiconductors

These are semiconductors in which certain amounts of impurities are purposely added to dilute the semiconductor material from its pure state. By doing this, they outperform intrinsic semiconductors regarding conductivity and properties. The substances are referred to as doping agents or dopants. P-type or n-type semiconductors are formed, respectively, when materials with three (trivalent) or five (pentavalent) electrons in their valence band are used as dopants on a tetravalent base material¹².

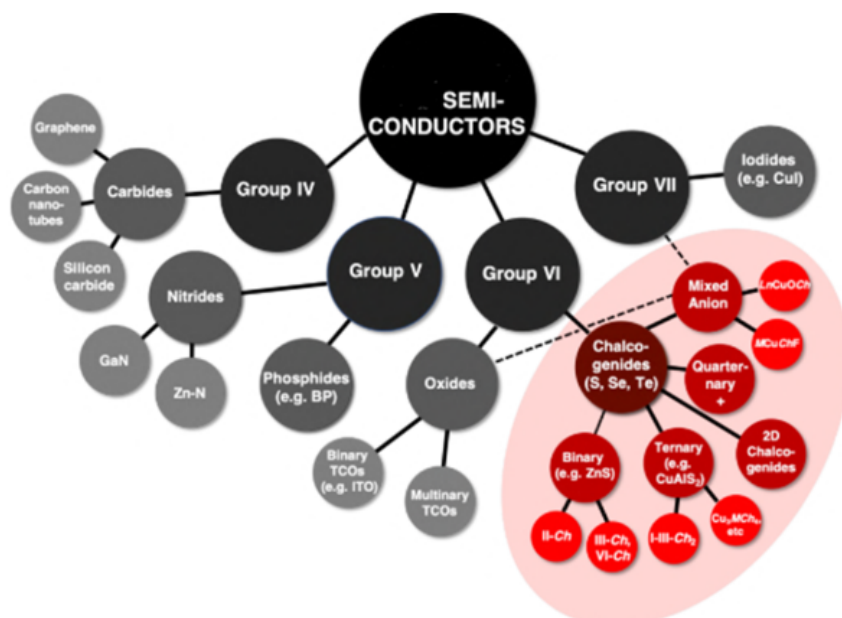


Figure 2.3: Classes of wide bandgap semiconductor materials shown in a schematic network diagram. A group of anions is used to classify the classes.¹⁴

Only three electrons are transferred from the trivalent atom, such as B, to the tetravalent atom, leaving one gap that needs to be filled with an electron. This is called a p-type semiconductor since it produces more holes than electrons. In p-type semiconductors, then, holes are the predominant charge carriers while electrons are the minority carriers. On the other hand, the electron is moved to the conduction band when a pentavalent dopant, like antimony, donates an extra electron in the crystal structure that is not needed for covalent bonding¹³. Since this electron is already excessive, it does not produce a matching hole in the valence band. As a result, when this material is doped, the base material has more electrons than holes, which is why it is referred to as an n-type extrinsic semiconductor. In an n-type, holes are minority current carriers, whereas electrons are the majority carriers. Overall, the Fermi level is located halfway between the conduction band and the valence band; for the n-type, it shifts upward, and for the p-type, it drifts downward¹³.

The red double arrow highlighted represents the wide band gap semiconductor nanoparticles in Figure 2.2. In contrast, two-dimensional semiconductor materials are showed in figure 2.3. There is a lot of interest in semiconductor nanoparticles for electronics, sensing, and light-harvesting devices because of their size-dependent nature, material tenability, and tolerability¹⁴.

2.1.3 Binary nanoparticles

This collection of semiconductor nanoparticles comprises both metallic and non-metallic elements. The metals mostly consist of the d-block elements, specifically groups III and the lower members of groups IV and V. Conversely, the non-metals primarily consist of elements from the earlier members of groups IV and V and elements from group VI. The materials encompassed in this list comprise but are not restricted to, cadmium selenide (CdSe), cadmium telluride (CdTe), zinc sulfide (ZnS), PbS, zinc oxide (ZnO), magnetite (Fe₂O₃), GaN, titanium oxide (TiO₂), SnS, Bi₂Se₃, and mercuric selenide (HgSe), among other substances¹⁵.

2.1.4 Binary metal oxides

Metal oxide nanoparticles are significant binary nanoparticles used across various technological domains. The oxides mentioned primarily occur in powers of 2 and 4, such as ZnO, NiO, SnO₂, CeO₂, TiO₂, Fe₂O₃, and MoO nanoparticles¹⁶. Their preparation necessitates a significant investment of time and energy. Various alternative synthetic approaches exist to produce these nanoparticles and precisely regulate the crystalline particles' size, shape, and arrangement. The oxides can be synthesized from metal precursors, such as acetates or acetylacetonate, in the presence of solvents, such as benzyl alcohol, using either microwave or autoclave heating methods¹⁷.

The methodology and precursor type selection significantly influence the dimensions and morphology of the nanoparticles. Nanorods, nanospheres, nanoflowers, nanohusks, nanocubes, and distorted cubes can be generated by modifying the precursors using straightforward, cost-effective, and environmentally friendly synthetic methods. Additional strategies that have been utilized include laser ablation technologies and biological production of metal precursors with reducing properties¹⁸.

TiO₂ nanoparticles

TiO₂ is a significant semiconductor nanoparticle with excellent catalytic capabilities, long-term stability, affordability, and non-toxicity. They are utilized as photocatalysts in water purification; however, their effectiveness is hindered by their large band gap between 3.2 eV and 3.35 eV and rapid charge recombination rate. When a semiconductor is exposed to light with energy higher than its band gap, there is a recombination process between electrons and holes. This interaction with the solution determines the catalytic process and the generation of redox species¹⁹. Nevertheless, it is possible to decrease the band gap energy and mitigate recombination processes in semiconductors by including materials capable of trapping electrons and holes²⁰.

ZnO nanoparticles

Zinc oxide (ZnO) is a versatile semiconductor material with a large energy gap of approximately 3.10 eV to 3.37 eV and a high exciton energy of 60 milli-electron volts (meV). ZnO nanoparticles have diverse applications in solar cells, UV lasers, light-emitting diodes, fuel cells, varistors, photo-detectors, phosphors, transparent conducting electrodes, surface acoustic wave devices, various sensors, piezoelectric transducers, and optical and electrical devices²¹. Zinc oxide (ZnO) is used in solar cells to enhance their performance by minimizing electron recombination. This is

achieved through its high charge carrier mobility at ambient temperature, which ranges from 115 to 155 cm^2 ²². Zinc oxide and its composites are commonly used as electrolyte membranes in low-temperature-solid oxide fuel cells, making them desirable for fuel cell technology. Fuel cells in this category demonstrate exceptional energy conversion efficiency, release minimal greenhouse emissions, and possess excellent fuel adaptability²³.

2.2 Chitin and Chitosan (Ch): molecular structures

Chitosan, often called deacetylated and soluble chitin, is an unbranched binary polysaccharide. It consists of N-acetyl-D-glucosamine and D-glucosamine; its chemical name is (1→4)-2-amino-2-deoxy-D-glucose. Chitosan is obtained by partially removing acetyl groups from the natural polysaccharide chitin. Chitin is mostly sourced from marine arthropods like shrimps and crabs²⁴.

2.2.1 Source

Chitin, the primary component of chitosan, is a natural polymer present in various organisms, including crustaceans, mollusks, algae, insects, and the cell walls of fungi²⁵. The chitin levels in these species vary as follows: Chitin content ranges from 15–30% in crab cuticles, 20–30% in crustacean exoskeletons, 30–40% in shrimp cuticles, 5–25% in insect cuticles, and 2–44% in fungal cell walls²⁶.

The chitosan utilized for industrial purposes primarily originates from crustaceans, particularly crab, prawns, and shrimp shells, easily accessible as waste products from the food processing industry. Nevertheless, it is progressively becoming more accessible as a by-product of the silk industry's cocoon breeding, as well as from extracting proteins from insects for the food and animal feed sectors and through fungal fermentation. Despite being composed of chitin, fish scales are frequently discarded due to their low yield, accounting for only 1% of their total weight²⁶. According to certain calculations, approximately 1012–1014 tons of chitosan derived from crustaceans are produced annually. The worldwide market for chitin and its derivatives reached a valuation of US\$2900 million in 2017, with a Compound Annual Growth Rate (CAGR) of 14.8%. The projected value is anticipated to reach US\$63 billion by 2024²⁴.

2.2.2 Production of Chitosan

Chitosan production involves several precise steps, starting with preparing chitin from biological material, followed by deacetylation to create chitosan. The production process for chitosan from crustacean shells typically consists of four essential steps: demineralization, deproteinization, decoloration, and deacetylation. These steps are necessary to extract a valuable biomaterial conveniently. The order of demineralization and deproteinization can be switched²⁷. The exoskeleton of crustaceans is commonly used as the initial material for commercial chitosan production. Figure 2.4 clearly illustrates the process of producing chitosan powder, which begins with extracting chitosan from crustacean shells.

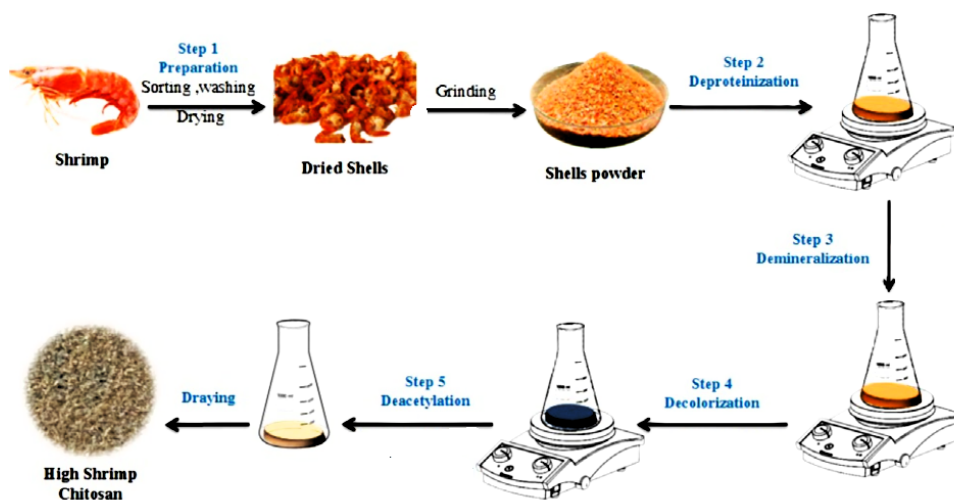


Figure 2.4: Steps to extract Shrimp chitosan.²⁶

2.2.3 Biosynthesis of chitosan

Chitosan exhibits a comparable molecular structure to that of cellulose. After removing the acetyl group from chitin, it becomes a linear polysaccharide with a complicated double-helix structure. This polysaccharide consists of (1,4)-2-acetamido-2-deoxy- β -D-glucose units as in Figure 2.5. The molecular weight typically ranges from 50 kilodaltons (kDa) to 2000 kilodaltons (kDa)²⁸. Chitosan is a plentiful natural polymer substance composed of monomer units connected by covalent glycosidic linkages. Chitosan possesses functional groups such as a primary hydroxyl group at the 6-position, a secondary hydroxyl group at the 3-position, and an amino group at the 2-position or certain N-acetylamino groups, together with glycosidic linkages. The NH_2 and OH groups in the chitosan molecule are highly reactive, allowing for the synthesis of several chitosan derivatives through reactions with various chemical groups that serve as the major groups for chemical modification. Nevertheless, the acetylamino and glycosidic bonds exhibit significant stability and resistance to breakage, posing challenges for chemical modification^{26,29}.

The degree of protonation of amino groups in the chitosan molecule increases proportionally with its DD (degree of deacetylation), resulting in enhanced solubility. The higher the molecular weight of chitosan, the greater the number of hydrogen bonds formed in its polymer chain, resulting in increased difficulty in dissolving. The viscosity of chitosan increases with higher molecular weight and concentration. Furthermore, the level of deacetylation also positively influences viscosity³⁰. An inherent issue in chitosan modification is the interference caused by the presence of OH or NH_2 groups, resulting in the introduction of undesired groups into the final product. Nevertheless, this issue can be circumvented by implementing protective groups. Hence, by altering reaction conditions and reagents, chitosan can undergo chemical modification in its amino, hydroxyl, or both amino and hydroxyl groups, forming N-modified, O-modified, or N,O-modified chitosan derivatives. Furthermore, the biological activity of chitosan and its derivatives is intricately linked to their molecular weight and deacetylation degree. Chitosan with a low molecular

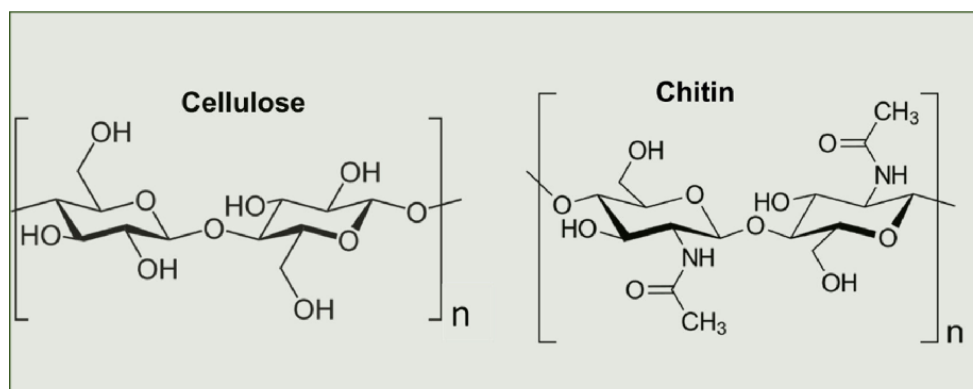


Figure 2.5: Structures of cellulose and chitin.²⁵

weight or a high degree of deacetylation typically exhibits more potent anticancer and antioxidant effects. In contrast, chitosan with a high molecular weight tends to possess better antibacterial capabilities³¹.

2.2.4 Physical properties of Chitosan

The degree of deacetylation, polydispersity, and molecular weight of chitosan are the primary factors that substantially impact its biological, physicochemical, and mechanical properties and, consequently, its application. DD and Mw influence a wide range of attributes, including solubility, reactivity, acid-base behavior, electrostatic behavior, flexibility, polymer conformation, viscosity, crystallinity, porosity, tensile strength, conductivity, ability to chelate metals, and photoluminescence³². Furthermore, the aforementioned parameters (DD and Mw) have an impact on various biological characteristics, including biodegradability, biocompatibility, mucoadhesion, hemostatic properties, analgesic properties, adsorption enhancement, antimicrobial activity, anticholesterolemic effects, and antioxidant properties. These properties are crucial in determining the material's suitability for specific applications³³.

Protonation of the $-NH_2$ group in chitosan allows it to interact with negatively charged derivatives, including proteins, dyes, enzymes, tumor cells, bacteria cell wall proteins, DNA, RNA, and other metal ions to create complexes. This interaction arises from the neutral or negatively charged hydroxyl groups of D-glucosamine. Under specific circumstances, its inability to dissolve in neutral solutions and its ability to dissolve in alkaline solutions make it a versatile polymer that can be used in polymer synthesis, as a solution, or as a solid polymer²⁶. In general, chitosan's resistance to enzymatic breakdown, particularly by lysozyme, is enhanced by a large concentration of acetyl groups. This characteristic makes it well-suited for the production of drug delivery systems³⁴. Despite its solubility in many organic solvents and weak organic acids solutions like acetic acid and formic acid, the limited solubility of chitin/chitosan in water has impeded its complete utilization. Consequently, numerous studies have been conducted to devise methods for improving the water solubility of chitosan³⁵.

2.2.5 Biological Sources of Composition:

The quality of the computer science end products is also contingent upon the composition of the source, which in turn affects its function in determining the application. Chitin obtained from marine biowaste commonly contains heavy metals such as nickel and copper. In contrast, CT derived from microbial sources consists of relatively pure CT molecules³⁶. Similarly, several proteins found in CT from the seafood sector and certain insects possess allergenic qualities that can trigger anaphylactic shock. As a result, their use in therapies is restricted³⁷.

The purity and concentration of CT and Ch play a crucial role in therapeutic applications. Chondroitin sulfate derived from fish is typically more concentrated and pure than derived from microbes. As a result, it is commonly favored for biomedical purposes³⁸.

Ch crystallinity:

Another crucial factor to consider when selecting CT for specific applications is the degree of crystallinity. The reactivity of β -Ch from squid pen surpasses that of α -Ch because of its hydrated structure and diminished intermolecular hydrogen bonding. Moreover, squid CT is highly advantageous for fabricating thin films and their application in biosensors³⁹.

Hybrid Composites

Titanium dioxide (TiO₂) and zinc oxide (ZnO) can be incorporated into different organic materials such as corn and potato starches, carboxymethylcellulose, sesame, whey proteins, wheat gluten, cellulose, poly-lactic acid, xanthan and gellan gums, and chitosan, either individually or in combination. The goal is to develop hybrid composites with possible industrial applications as indicated in Table 2.1.

2.3 Mott conduction

Mott conduction, a fundamental aspect of condensed matter physics, is observed in disordered systems where charge transport occurs via phonon-induced tunneling of electrons between localized states. This phenomenon is characterized by a temperature-dependent electrical conductivity formula derived by Mott, indicating the significant role of electron localization and electron-phonon interactions in these materials⁴¹. Studies on semiconducting oxide glasses have also confirmed the applicability of Mott's theory, where the polaronic hopping model describes electrical transport, albeit with some deviations observed in phase-separated glasses⁴². Further research has explored the intricate relationship between Mott insulating states and conductivity, revealing that strong interactions can suppress conductivity due to interactions rather than band filling. This has been observed in various materials, including fermionic atoms in optical lattices, showcasing the Mott insulator phase's emergence due to repulsive interactions⁴³. Moreover, the dynamic response of Mott insulators to electric fields has been a subject of interest, revealing potential pathways for the electric breakdown of Mott insulators through field-induced insulator-to-metal transitions, highlighting the complex interplay between electronic structure and external perturbations⁴⁴.

Table 2.1: Application of some polymers and proteins functionalized with TiO₂ nanoparticles.⁴⁰

Material	Application
Corn starch	Bioplastic with potential use as packaging material
Carboxymethyl cellulose containing miswak extract	Nanocomposite with potential use as food packaging
Sesame protein extract	Films for food active packaging applications and photo-decolorization purposes
Corn starch/PVA	Potential application in food and non-food industries as UV shielding packaging materials
Chitosan/potato-starch	Films with potential use as food packaging
Chitosan/starch	Films with potential use as food packaging
Cellulose	Removal of water pollutants
Bi ₂ WO ₆ -TiO ₂ /corn starch	Films with ethylene scavenging activity, potential use for fruits and vegetables preservation
KC/X/G	Potential application in food and non-food industries as UV shielding packaging materials
Alginate	Removal of water pollutants
Potato starch	Films with potential use as food packaging
Amylose-halloysite composite	Composite with potential environmental applications as wastewater treatment
Wheat/cellulose	Films with antibacterial properties
Corn starch/PVA	Nanocomposite with potential use as packaging material
Alginate	Medical applications as tissue regenerator
Poly(L-lactic acid)	Potential use as drug delivery system
Whey protein	Biopolymer with potential use as packaging material
Hydrophilic polyurethane	Films with antibacterial properties

ZnO and TiO₂ are semiconducting materials known for their high electron mobility and photocatalytic properties. When embedded in a chitosan matrix, these nanoparticles can create form a good mott conduction for electrons, thereby enhancing the electrical conductivity of the composite. The semiconductive nature of these nanoparticles allows for the generation and transport of charge carriers under specific conditions, such as UV light exposure, which can increase the overall conductivity of the material compared to pure chitosan, which is an insulator⁴⁵. The photocatalytic activity of ZnO and TiO₂ under UV light can also contribute to enhanced conductivity in the composite. These nanoparticles can generate electron-hole pairs upon UV irradiation, where the electrons can contribute to the material's conductivity. This effect can be particularly significant in applications where UV exposure is utilized, leading to a dynamic increase in conductivity in response to light exposure⁴⁶.

The interface between ZnO or TiO₂ nanoparticles and the chitosan matrix is critical in affecting the composite's conductivity. The distribution, size, and surface modification of the nanoparticles can influence the extent of interfacial interaction with the polymer matrix, thereby affecting the mobility of charge carriers and the overall electrical properties of the composite. Proper dispersion and interaction of nanoparticles within the matrix are crucial for enhancing conductivity⁴⁷. Also, there is an optimal concentration at which the conductivity reaches a maximum, beyond which further increases in nanoparticle content can lead to aggregation and decreased efficiency of charge transport pathways. Another topic is the morphology and distribution of the nanoparticles within the chitosan matrix that can play a critical role in affecting the photoconductance. Uniform distribution and optimal NPs size can enhance the surface area for light absorption and charge carrier generation. Moreover, the specific surface morphology of nanoparticles can influence the scattering and trapping of light within the composite, potentially leading to enhanced light absorption and photoconductivity⁴⁸.

This combination also leads to synergistic effects that further enhance the photoconductance. The different energy band alignments of ZnO and TiO₂ can facilitate a more efficient separation of charge carriers and extend the light absorption range, contributing to a higher photoconductivity under a broader light spectrum. This synergy can be particularly beneficial in photocatalytic applications where a wide range of light absorption is desired⁴⁵.

2.3.1 Chitosan/TiO₂ Composite

The Ch/TiO₂ hybrid composite is acknowledged as a very promising material due to its diverse applications, particularly its exceptional structural, textural, mechanical, and optical properties. Additionally, it can act as an effective barrier against water and oxygen while demonstrating remarkable thermal stability and biodegradability. The impact of incorporating TiO₂ into a Ch matrix on the aforementioned attributes has been thoroughly investigated in this particular context. The addition of TiO₂ enhances the structural characteristics of Ch, resulting in increased dispersion and homogeneity on the surface of the Ch films. This is achieved by increasing the roughness and porosity of the films^{49,50}. Conversely, the addition of TiO₂ caused the crystalline peak of Ch to become wider, reducing the crystallinity of the Ch/TiO₂ composite. This suggests a significant interaction between TiO₂ and Chitosan⁴⁹.

The Ch/TiO₂ composite exhibited a type II isotherm, suggesting that the material possesses a macroporous structure⁵¹. However, the characteristics related to the texture of the Ch/TiO₂ composite, such as the specific surface area (SSA), pore volume, and pore size, were modified by the amount of TiO₂ used. For example, a higher

concentration of TiO_2 resulted in an increase in the SSA of the hybrid composite⁵². The alterations in the structural and textural characteristics of CS/ TiO_2 composites make them suitable for photocatalysis research.

2.3.2 Chitosan/ZnO Composite

Ch/ZnO composites have attracted interest due to their photocatalytic capabilities, which are crucial for applications like environmental remediation and antimicrobial treatments. Combining chitosan, a natural polymer, with ZnO nanoparticles improves the ability to use light to break down contaminants, resulting in more effective degradation of pollutants. An example is a study emphasizing the improved photocatalytic breakdown of malachite green dye when exposed to visible light using Ch/ZnO⁵³.

Additional investigation into Ch/ZnO composites has unveiled their multifunctional capacities, expanding beyond their use in photocatalysis to encompass antimicrobial properties. A notable research work documented the production of Ch/ZnO hybrid composites using a chemical precipitation technique. When exposed to UV light, these composites demonstrated remarkable photocatalytic activity in breaking down methylene blue dye and exceptional antibacterial effectiveness against *Escherichia coli*. The ability of Ch/ZnO composites to serve two purposes emphasizes their potential as environmentally friendly and cost-efficient materials for various uses, such as water treatment and antimicrobial coatings. This highlights their versatility and suitability for addressing environmental and public health challenges⁵⁴. Ch/ZnO composites have been investigated for their application in bio-finishing procedures in industrial settings, namely for improving the characteristics of cotton fabrics. A prominent study showcased the production of Ch/ZnO composites using a hydrothermal technique. This method not only improved the heat resistance of the treated fabrics but also provided them with considerable antibacterial properties⁵⁵.

Chapter 3

Methodology

3.1 Reagents and Equipment

3.1.1 Equipment

The research employed sophisticated equipment to synthesize, characterize, and analyze the TiO₂-ZnO-chitosan composite films. The Mini-flex-600 X-ray Diffractometer is used to determine the crystal structure of nanoparticles. Optical properties were analyzed using a UV/Vis/NIR LAMBDA 1050 Spectrophotometer. The dispersion of nanoparticles was facilitated by a SONOPLUS Bandelin Ultrasonic Homogenizer Mini20. Precise mass, pH, and conductivity measurements were taken using an Analytical Balance HR-150A from COBOS and a 914 pH/Conductometer from Ω Metrohm. The mixture was heated and stirred using a hot and stirrer Plate TOPO. Centrifugation was performed with a Sorvall Legend XTR Centrifuge from Thermo Scientific, and drying of samples employed a FreeZone Lyophilizer. Dynamic Light Scattering (DLS) Brookhaven BIC 90 Plus was crucial for measuring the particle size distribution and zeta potential of the nanoparticles in solution, ensuring uniformity in the composite preparation. Also, the NX7 AFM by Park System Atomic offered nanoscale imaging of the films' surface topography and morphology, providing vital data on film uniformity and nanoparticle distribution. Finally, a homemade circuit followed by the DAQ "NI USB-6210".

3.1.2 Materials and chemicals

The composite films comprised Chitosan of medium molecular weight and Titanium Dioxide (TiO₂) obtained from Sigma-Aldrich. The materials were chosen for their high purity and suitability for research purposes. Sodium carbonate and Zinc Nitrate solutions are used to produce Zinc Oxide (ZnO). The study employed a range of high-quality chemicals, such as Glacial Acetic Acid for dissolving chitosan, Absolute Ethanol for cleansing substrates, Sodium Hydroxide for pH adjustment, and Sodium Chloride to ensure uniformity and dependability across all experimental protocols. The study utilized distilled water as the preferred solvent for all processes in order to prevent

the presence of any impurities.

3.2 Fabrication of Interdigitates

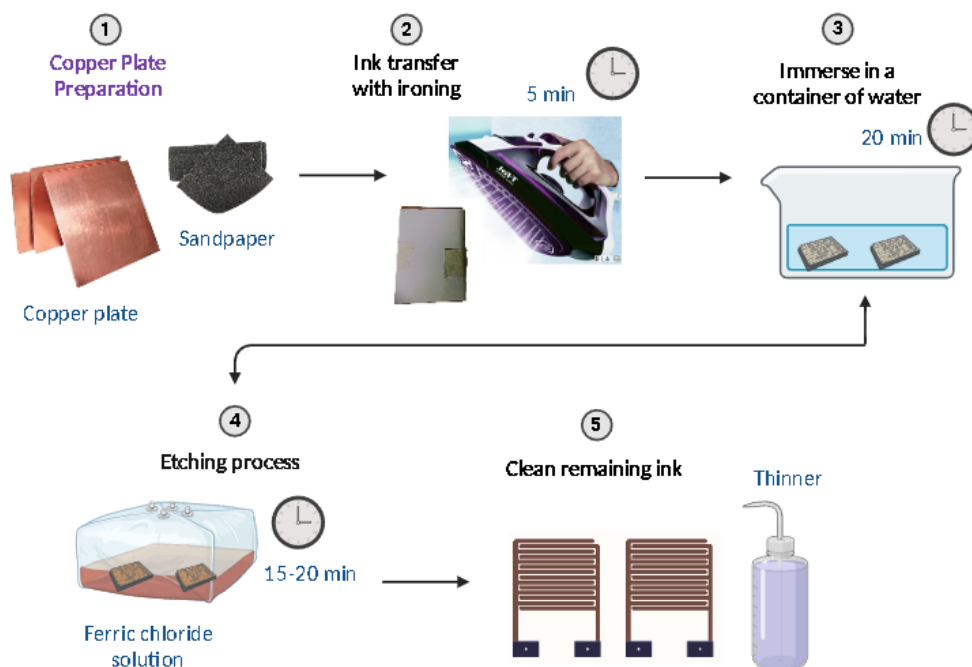


Figure 3.1: Graphical scheme of the steps to follow for fabrication of interdigitates.

The fabrication of the copper interdigitates for this study followed a meticulous process to ensure the accuracy and quality of the pattern, as shown graphically in Figure 3.1. First, we made the design in a PCB wizard, adjusting the desired sizes for the project. Then, a copper plate was cut, and its irregular edges were sanded using alcohol and a 600-grit water sandpaper. This step was crucial for adequately preparing the surface. Subsequently, the couche paper with the required laser printer paint line pattern was cut to the appropriate dimensions. Care was taken not to touch the laser printer paint on the paper. The copper plate was then positioned over the inked section, and the ends were folded to the rear, securing them with tape to maintain the position. The next stage involved ironing the copper surface for at least 5 minutes using the wool setting on a standard iron, allowing the ink to adhere firmly. After this step, the plate was immersed in a water container, waiting for the water to cover the paper completely and the ink to become clearly visible. The paper was delicately removed, preventing the ink from spreading. The plate was air-dried, and the quality of the ink pressing was verified. Subsequently, the plate was submerged in a ferric chloride solution, continuously agitating it for at least 15 minutes. This process dissolved the unnecessary copper from the pattern, ensuring only the ink remained intact. After confirming the plate's condition was suitable, with the excess

copper removed, the ink was rigorously cleaned with thinner to achieve the desired copper pattern. Finally, the pad section was soldered, completing the fabrication of the interdigitates with the specific pattern required for this study.

3.3 Synthesis of TiO₂ Nanoparticles

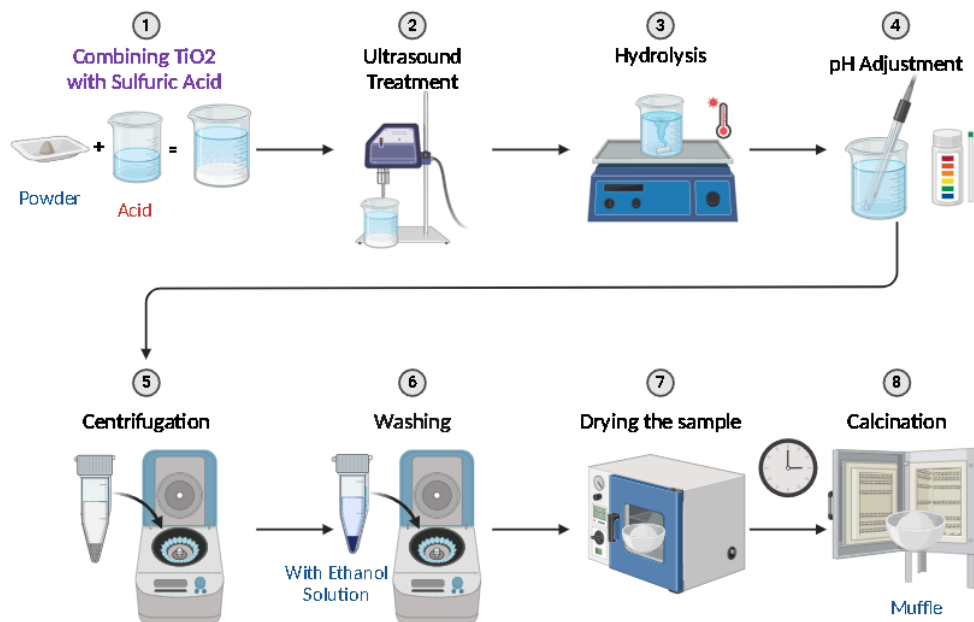


Figure 3.2: Graphical scheme of the steps to follow for TiO₂ synthesis.

The synthesis of titanium dioxide (TiO₂) nanoparticles was prepared using 10 g of TiO₂, which were added to 40 mL of sulfuric acid. The ultrasound method treated the mixture using a *Sonoplus ultrasound homogenizer mini 20* equipment. Using ultrasound in these samples is beneficial for inducing chemical dynamic alterations to produce new precursors for further synthesis. The ultrasound equipment was set with a nominal ultrasonic output of 20W, a pulse level of 50.5 s, and an amplitude of 80%. Three ultrasound interactions, each lasting 15 minutes with a rest period of 5 minutes between them, were performed on the sample. Subsequently, the sample was hydrolyzed with distilled water at 100 for 1 hour. The pH of the compound was then adjusted to a range of 8 to 11 using a sodium hydroxide solution.

A centrifuge separation process, followed by a thorough washing with distilled water, was carried out to remove all by-products from the sample. The sample was then dried for 24 hours at 50. Finally, an annealing process to restore the crystalline structure of TiO₂ was conducted using a muffle at 500 for two hours in an air atmosphere⁵⁶. The process is detailed in the Figure 3.2 and the reactions leading to the formation of nanostructured TiO₂ are detailed in the equations of figure 3.3

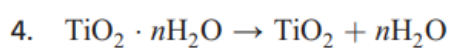
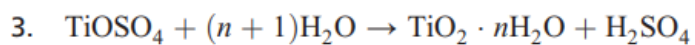
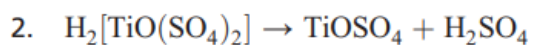
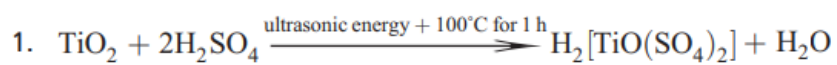


Figure 3.3: Chemical reactions occurring in each process of the synthesis.⁵⁵

3.4 Synthesis of ZnO nanoparticles

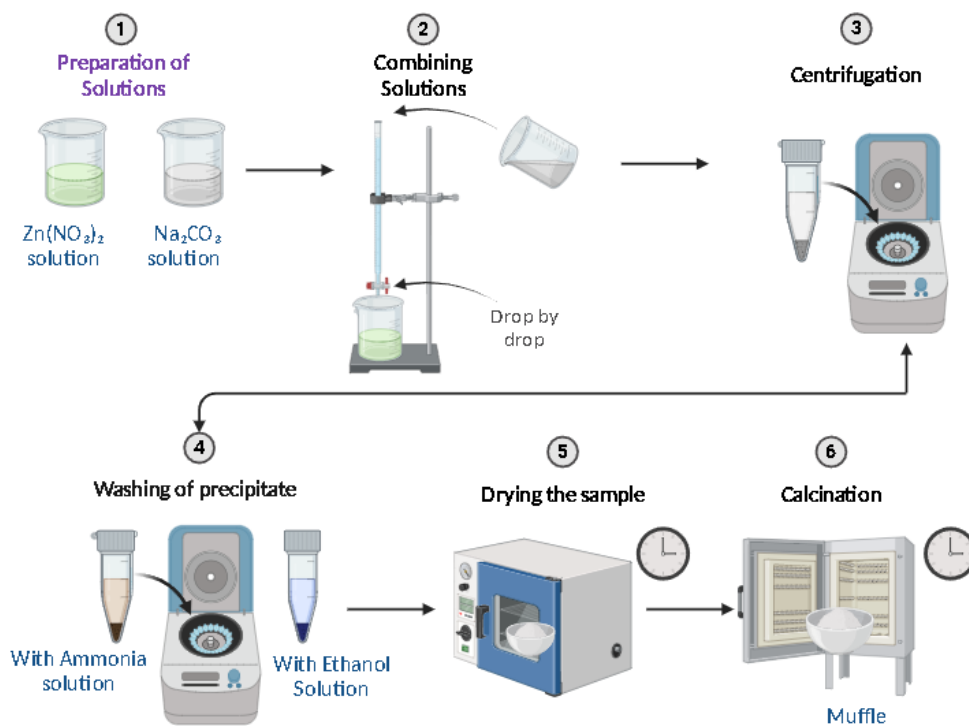


Figure 3.4: Graphical scheme of the steps to follow for ZnO synthesis.

Zinc oxide nanoparticles were synthesized, scaling the procedure to accommodate a 1 g reaction scale based on methods reported by Wang et al.⁵⁷. Zinc nitrate and sodium carbonate solutions were prepared at a concentration of 0.05 M. To suit the larger scale, the volumes of the solutions were adjusted: 200 mL for zinc nitrate and 300 mL for sodium carbonate. The synthesis began by placing 200 mL of zinc nitrate solution in a larger beaker under continuous stirring to ensure a homogeneous mixture. Then, 300 mL of sodium carbonate solution was added gradually to the beaker. The careful addition of sodium carbonate led to a whitish precipitate, indicative of nanoparticle synthesis. Following the reaction, the mixture was transferred into larger Falcon tubes for centrifugation at 10000 rpm for 5 minutes. This step was essential for separating the nanoparticles from the liquid phase. The supernatant was then decanted, leaving behind the solid precipitate.

The washing of the precipitate involved using 0.1 M ammonia solution. The precipitate was dispersed in the solution by shaking and centrifugation under the same conditions. The supernatant was removed after centrifugation. This process was repeated with ethanol, following the same steps as the ammonia wash. Finally, the nanoparticles were dried on a larger watch glass at 80 °C for 4 hours and subsequently calcined at 250 °C for 3 hours. This methodology effectively facilitated the synthesis of a larger quantity of zinc oxide nanoparticles, emphasizing optimal particle formation and purity. The process is detailed in Figure 3.4.

3.5 Characterization Techniques

3.5.1 Ultraviolet-Visible-Near Infrared Spectroscopy (UV/Vis/NIR)

The sample's optical transmittance was quantified using a LAMBDA 1050+ UV/Vis/NIR Spectrophotometer (PerkinElmer, Waltham, MA, USA) at a scanning speed of 50 nm/s across the 250–800 nm wavelength range. Analyzing the optical properties of TiO₂ and ZnO NPs involved using the reflectance of UV (200 nm) to visible (700 nm) regions.

3.5.2 X-Ray Diffraction (XRD)

The XRD analysis for Nanoparticles was recorded with the Rigaku Miniflex 600 X-ray diffractometer. It features a 600W X-ray tube and a Bragg-Brentano goniometer with an 8-position auto-sampler. It employs the D/tex Ultra detector and SmartLab Studio II software. Under the specified measurement conditions, the X-ray generator operates at 40 kV and 15 mA, utilizing a CuK(α) sealed tube as the radiation source. Data acquisition uses a Theta/2Theta scanning axis with a 0.01° step size. The scanning range covers 10° to 100° in 2Theta, and the D/tex Ultra2 detector is employed in 1D scanning mode.

3.5.3 Dynamic Light Scattering (DLS)

Dynamic Light Scattering (DLS) analyzed particle size and distribution using a Brookhaven BIC 90 Plus particle size analyzer. This instrument is adept at handling diverse sample types, predominantly nanoparticles and colloidal-sized materials in non-absorbing liquids. The analyzer has the capability of detecting particle sizes ranging from 0.3 nm

to 10 μm , with the specific range dependent on the refractive index and concentration of the sample. For signal processing, the system utilizes DLS with a standard accuracy deviation typically within $\pm 1\%$. Featuring an integrated temperature control system, the analyzer operates within a range from -5°C to 110°C , with an accuracy of $\pm 0.1^\circ\text{C}$, thereby obviating the need for an external temperature circulator. The Brookhaven BIC 90 Plus is equipped with a red diode laser, providing a stable and precise light source for DLS measurements, which is essential for the accurate determination of particle size distribution.

3.5.4 Atomic Force Microscopy (AFM)

The surface topography of nanoparticles into the chitosan matrix was characterized using the NX7 Atomic Force Microscope (AFM) by Park Systems. Measurements were conducted in tapping mode, employing a PPP-NCHR type cantilever with a nominal length of 125 μm , mean width of 30 μm , thickness of 4 μm , a resonance frequency of 320 kHz, and a force constant of 42 N/m. Z-height images were acquired with a resolution of 1024x1024 pixels, covering a scan area of 1x1 μm^2 . The scanning rate was set to 0.2 Hz, with a Z servo gain of 2.418E3 nm and a set point of 5.04E3 nm. The selected frequency for acquisition was 293.183 Hz, with a driving amplitude of 0.89%. These parameters were optimized to yield high-resolution images enabling detailed assessment of nanoscale surface morphology.

3.6 Dilution of Chitosan

Preparation of 1% Chitosan Dissolution in Acetic Acid:

In a 250 ml beaker, 198 ml of distilled water was accurately measured using a graduated cylinder. The measured water was gently poured into the beaker. Next, 2 ml of glacial acetic acid was added to the water using a graduated pipette to achieve a 1% acetic acid concentration. A magnetic stirrer was used to ensure thorough mixing and homogeneity of the solution. The mixture was methodically stirred until complete homogeneity was achieved. This meticulous process ensured the successful preparation of a 1% chitosan solution in acetic acid, laying the groundwork for the subsequent phases of the research.

Adding Chitosan:

After the 1% acetic acid solution was prepared, diluting the chitosan to 1% concentration was next. Based on information from various sources, we found that chitosan with a medium molecular weight is the most optimal for the study of photoconductance; then, 2 grams of powdered chitosan were meticulously weighed using an analytical balance. Subsequently, the weighed chitosan was added to 200 ml acetic acid solution. A magnetic stirrer was employed to thoroughly mix the chitosan with the solution, accompanied by a glass rod to mix any excess material on the surface. The stirring continued until the chitosan was completely dissolved, and a clear, homogeneous solution of 1% chitosan in acetic acid was obtained. This dissolution process can take approximately one hour to achieve clarity and homogeneity. The resulting 1% chitosan solution in acetic acid is a crucial component for subsequent stages of research, especially in film fabrication.

3.7 Preparation of Ch/TiO₂ solution

Moving on to creating films, solutions with varying concentrations were prepared. The initial focus was utilizing TiO₂ nanoparticles, with concentrations ranging from 0.01% to 0.7% w/v. Given that only a minimal amount of solution was required for each film, a modest volume of 10ml was used for each concentration. This comprised 8 ml of the previously diluted chitosan solution and 2 ml of distilled water.

The specific concentrations selected for the Ch/TiO₂ solutions were 0.01%, 0.1%, 0.3%, 0.5%, and 0.7% w/v. This careful selection aimed to explore a range of concentrations to study their impact on the properties of the resulting films. The meticulous preparation of these Ch/TiO₂ solutions laid the groundwork for the subsequent fabrication of films with distinct Ch/TiO₂ concentrations, contributing to the comprehensive characterization of photoconductance in the research study.

As an illustration, the formulation of the 0.1% w/v Ch/TiO₂ solution involved precise steps for optimal dispersion. For this concentration, 10 milligrams of TiO₂ nanoparticles were measured. A 25ml beaker was utilized to streamline the process. The mixture was subjected to ultrasonication to achieve a uniform dispersion of nanoparticles. A laboratory stand with clamps was employed to secure the ultrasonic probe in place. The ultrasonic treatment was then initiated with an amplitude set at 90%, without intervals. Initially, the TiO₂ nanoparticles were introduced into the beaker, and for effective dispersion, 2ml of distilled water was added and taken to ultrasound for 5 minutes, ensuring the absence of agglomerations and promoting a homogeneous distribution. Subsequently, 8 ml of the diluted chitosan solution was added. The entire mixture underwent continuous ultrasonication for an extended period of 10 minutes, ensuring complete homogeneity. Upon completion, the solution was sealed and labeled for storage until use. It is recommended to utilize the solution promptly after sonication to maintain its optimal properties. This meticulous preparation served as a template for creating Ch/TiO₂ solutions with varying concentrations, contributing to the overall success of film fabrication for subsequent experiments.

3.8 Preparation of Ch/ZnO solution

For the fabrication of the Ch/ZnO films, solutions with varying concentrations (0.01%, 0.1%, 0.3%, 0.5% and 0.7% w/v) were prepared, each also with a minimum volume of 10 ml. A distinct step in this process was the addition of 2 ml of 20% acetic acid to the ZnO solution, which is a complicated oxide that does not disperse in water. The remaining 8 ml consisted of the diluted chitosan solution.

For example, for the 0.1% w/v concentration, 0.01 g of ZnO nanoparticles were measured. A 25 ml beaker was used for optimization and convenience. The ZnO nanoparticles and the solution were introduced into the beaker. The mixture was then subjected to ultrasound using a laboratory stand with tongs and an ultrasonic probe set to an amplitude set at 90%, with no intervals.

The process continued with the addition of 2 ml of 20% acetic acid. This mixture was subjected to ultrasound for 5 minutes, ensuring homogeneous distribution without agglomeration. Next, 8 ml of the diluted chitosan solution was added. This was followed by continuous ultrasonication for an extended period of 10 minutes, ensuring complete homogeneity. Once complete, the solution was sealed and labeled for storage until use. It is recommended that the

solution be used immediately after sonication to maintain its optimal properties. This detailed preparation process was a guideline to create Ch/ZnO solutions with different concentrations, contributing to the tests' success.

3.9 Preparation of Ch/TiO₂/ZnO solution

Solutions of different concentrations (0.01%, 0.1%, 0.3%, 0.5% and 0.7% w/v) were generated using a modest volume of 10ml for each concentration in order to fabricate Ch/TiO₂/ZnO films. In line with the Ch/ZnO preparation, 2 milliliters of 20% acetic acid were added to ZnO, an oxide not soluble in water, and the remaining 8 milliliters were made up of the diluted chitosan solution.

For example, 5 milligrams of ZnO and 5 milligrams of TiO₂/ nanoparticles were employed at a 1% w/v concentration. We used a 25 ml beaker for convenience and efficiency. The nanoparticles and 2ml of 20% acetic acid were put into the beaker to encourage dispersion. Using a laboratory stand with clamps and an ultrasonic probe with an amplitude set at 90%, the mixture was subjected to continuous ultrasonication.

The nanoparticles were first dispersed in 2ml of 20% acetic acid to guarantee homogeneity for five minutes. The diluted chitosan solution was added in an amount of 8 ml. After that, continuous ultrasonication was used for 15 minutes to guarantee total uniformity. The solution was finished and labeled before being stored until needed. To preserve the solution's best qualities, use it as soon as possible following sonication, just like earlier preparations. The careful preparation procedure helped fabricate films successfully for the experiments, which provided a framework for creating Ch/TiO₂/ZnO solutions at different concentrations. In figure 3.8, we can observe the chronological and detailed diagram of the steps to obtain the different solutions.

3.10 Film Fabrication on Interdigitated Electrodes:

To create films on the interdigitated electrodes, a meticulous process was followed to ensure proper dispersion and control during subsequent measurements:

Each interdigitated area was carefully delimited with tape to facilitate the correct solution dispersion without excess, allowing for precise measurements without interference with the electrodes. The film fabrication occurred in an area accessible to sunlight, ensuring correct drying. A flat surface with a stable base was chosen and secured with tape to prevent movement during the procedure. After organizing and labeling each sample and concentration, the solutions were prepared, ensuring clarity and avoiding confusion. Using a pipette, 3 drops of the solution were carefully placed on the interdigitated area. A glass slide was then employed to disperse the solution uniformly within the taped boundaries. The samples were left in a location with access to sunlight for 20 to 30 minutes, depending on the sunlight intensity. Care was taken to prevent the destruction or disintegration of samples containing TiO₂ due to prolonged exposure. After drying, the films were transported to a room with ambient temperature. The tape was delicately removed, and the film's quality was assessed. Subsequently, the films were securely stored in a sealed location for later measurements, ensuring the integrity of the samples until further analysis. The process to be followed with the solutions and the interdigitate can be seen in figure 3.5.

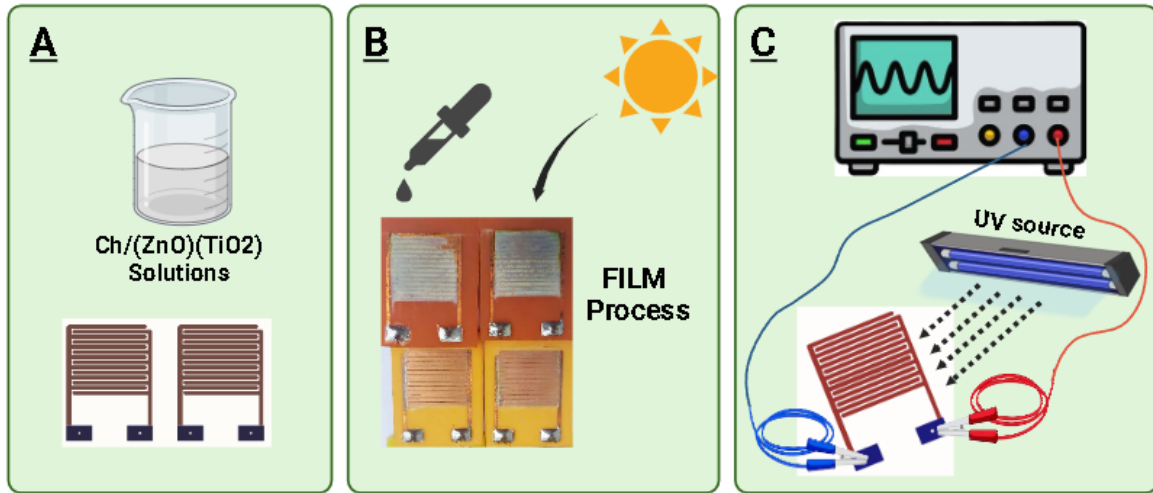


Figure 3.5: Representation for the process of the films, A) the materials required, B) drop-by-drop films before sun drying, and C) the measurement of each of the composites.

3.11 Equipment for measurements

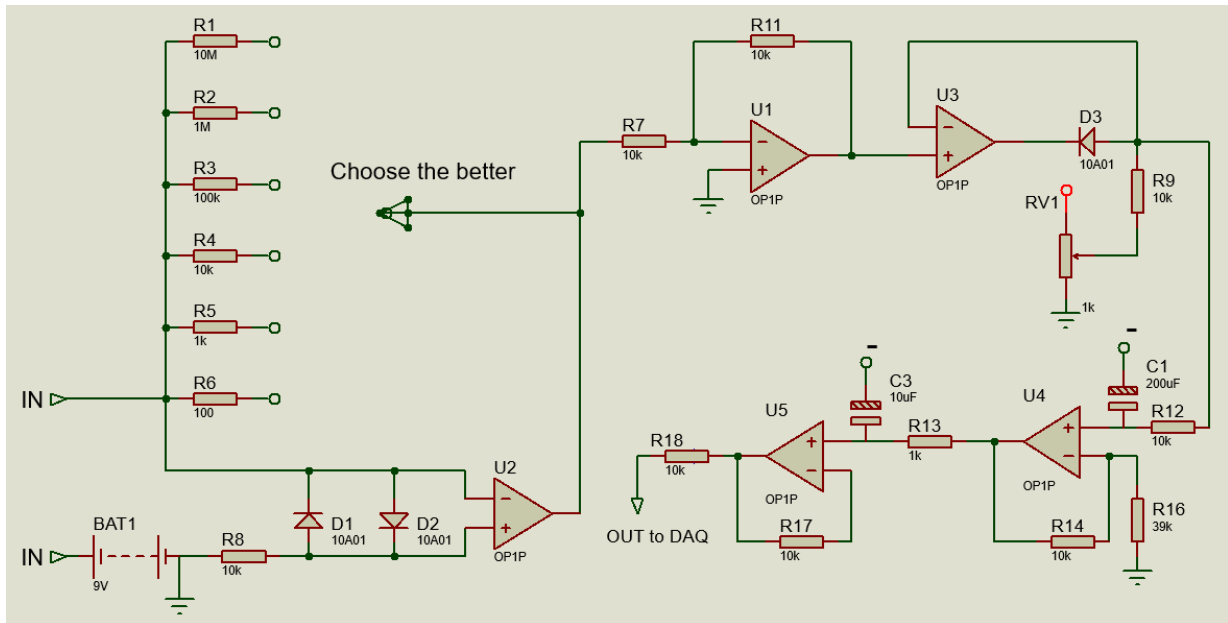


Figure 3.6: Graphical representation of the circuit used created in "Proteus" to verify its operation.

The circuit diagram in Figure 3.6 represents a customized setup designed to measure low currents. This circuit is suitable for this type of measurements with low range of photoconductance in interdigitated. The input, in this case, the interdigitate, is connected to a voltage divider network comprising a series of resistors (R1 through R6) that adjust the input signal level. This allows for the fine-tuning of the voltage applied across the interdigitated electrodes. The signal is then fed into an operational amplifier (U1), configured as a voltage follower to buffer the input signal and provide high impedance. The buffered signal passes through a diode protection network (D1 and D2) that guards the subsequent operational amplifier (U2) against potential voltage spikes. U2, in a non-inverting amplifier configuration, further amplifies the signal with the feedback provided by R7 and R11. The amplified signal is then processed through a second amplification (U5) stage, where the gain can be finely adjusted using the potentiometer RV1, to match the dynamic range of the data acquisition (DAQ) system. The output of U5, representing the photoconductance, is directed to the DAQ system for recording and analysis. The DAQ system digitizes the analog signal into a digital format for further processing by a computer. The entire circuit is powered by a 9V battery (BAT1), ensuring a stable and noise-free power supply.

The images in Figure 3.7 depict a custom-built measurement setup designed for assessing the photoconductance properties of chitosan/TiO₂/ZnO composite films. The top-left image shows the interdigitated electrodes, the core components where the composite films are deposited. These electrodes are mounted on an insulating base, ensuring that the measured conductance is solely due to the film's response to the UV source between 320 y 450 nm. Then, after that, there is the UV light source, indicated by the blue object, which is crucial for photoconductivity tests. It enables the study of the composite films under UV irradiation, thus simulating real-world conditions where these materials could be used in devices that leverage their photoresponsive properties. the bottom-right image shows the homemade electronics setup, including variable resistors, potentiometers, and other components explained in the circuit. Finally, the bottom-left image features a National Instruments Data Acquisition (DAQ) device, a component that interfaces the physical signals from the electrodes with the digital processing system. This device converts the analog signals of electrical conductance into digital data that can be analyzed on the computer.

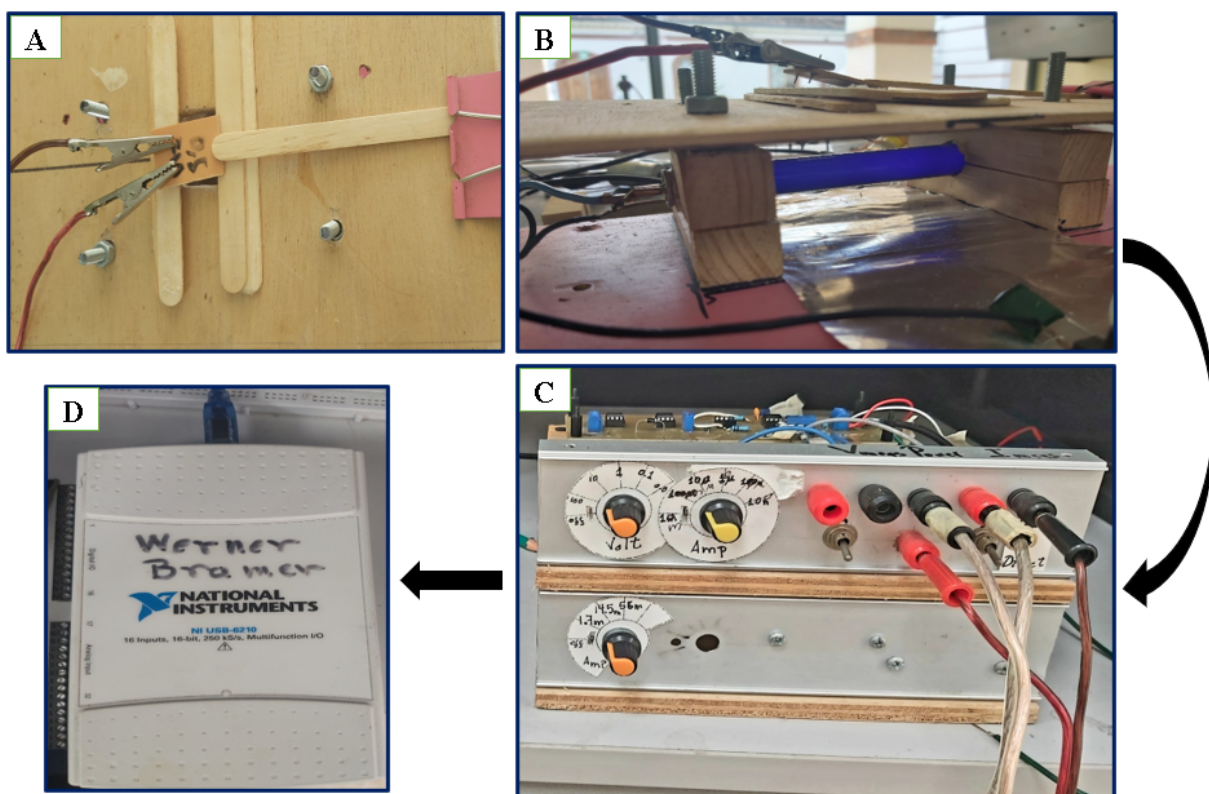


Figure 3.7: Homemade measuring equipment, A) connection of the electrodes to the interdigitate seen from above, B) base created including the UV source seen from the front, C) external circuit with its modifiable resistance, D) DAQ system.

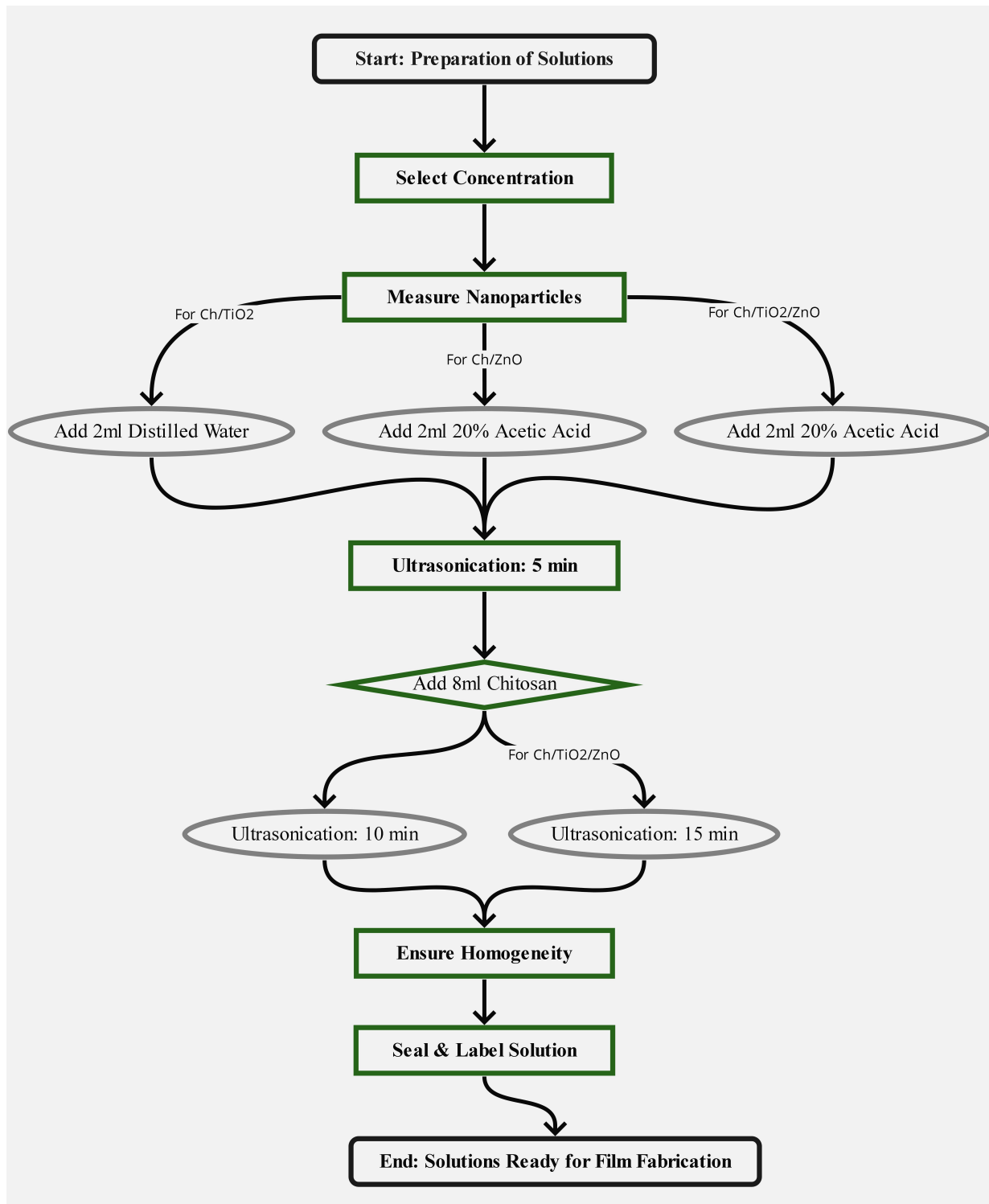


Figure 3.8: Scheme of the steps to follow for the realization of each one of the solutions, taking into account the respective changes in each one.

Chapter 4

Results & Discussion

4.1 Interdigitates obtained and their scale

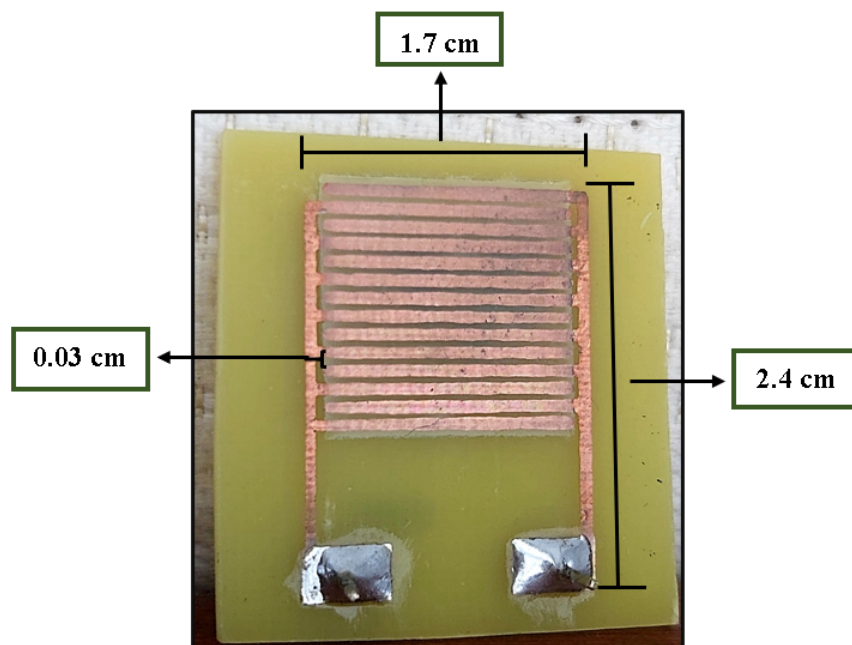


Figure 4.1: Interdigitated developed with respective reference measurements, the height, the width and the electrode spacing.

The provided image in figure 4.1 offers a detailed view of the interdigitated electrode with specific dimensions

annotated, which is fundamental for assessing the photoconductance properties of the semiconductor films applied to it. The dimensions, particularly the width of the gaps between the electrodes (0.03 cm) and the overall active area defined by the length (1.7 cm) and width (2.4 cm) of the electrode array are critical for quantifying the photoactive region and ensuring uniform application of the semiconductor films.

The compact size of the electrode, combined with the precise gap width, allows for a controlled and consistent application of the Ch/TiO_2 and Ch/ZnO composites, ensuring that each film experiences the same electrical environment during testing. This uniformity is essential for comparing the intrinsic photoconductance properties of the materials without interference from varying electrode geometries.

4.2 TiO_2 nanoparticles obtained

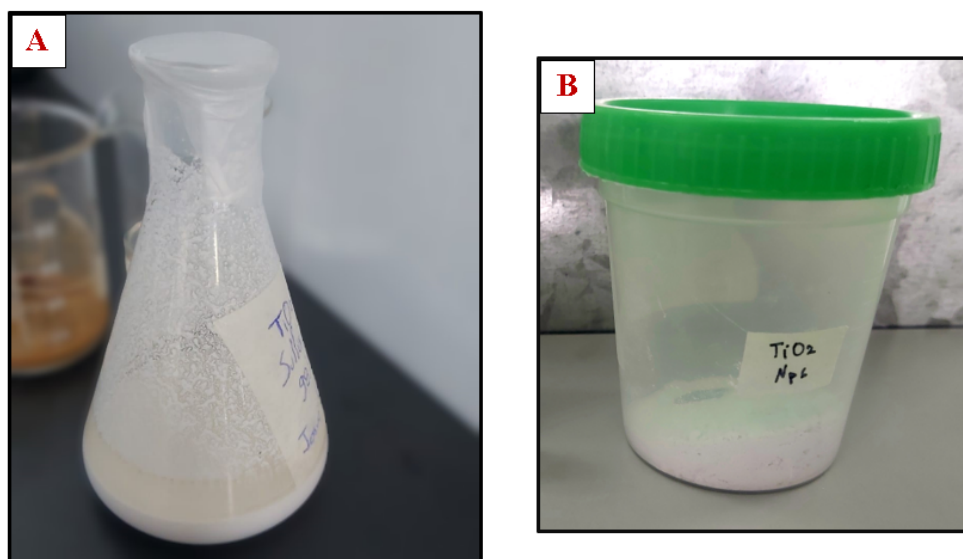


Figure 4.2: Results of the TiO_2 nanoparticles synthesis with A) The solution obtained from the synthesis and B) the TiO_2 powder obtained after the calcination process.

The material characterization process meticulously documented the physical appearance of the TiO_2 nanoparticles in solution and powder form showed in Figure 4.2. The pre-centrifugation solution displayed a uniform translucency, indicating a well-dispersed colloidal system. This homogeneity is critical for ensuring consistent centrifugation results, where the nanoparticles' separation is based on their mass and density. The solution's clarity, without any visible sediment or agglomeration, suggests effective nanoparticle distribution, which is essential for the accurate downstream application of these materials.

Upon observation, the TiO_2 nanoparticles exhibited a fine, homogeneous white powder housed in a clearly labeled container in their dry state. The powder's good physical appearance—free from clumping and impurities—points

to a high-quality synthesis process. Such a fine and even texture is desirable for photocatalytic applications, where surface area and particle-to-particle consistency significantly impact performance.

4.3 ZnO nanoparticles obtained

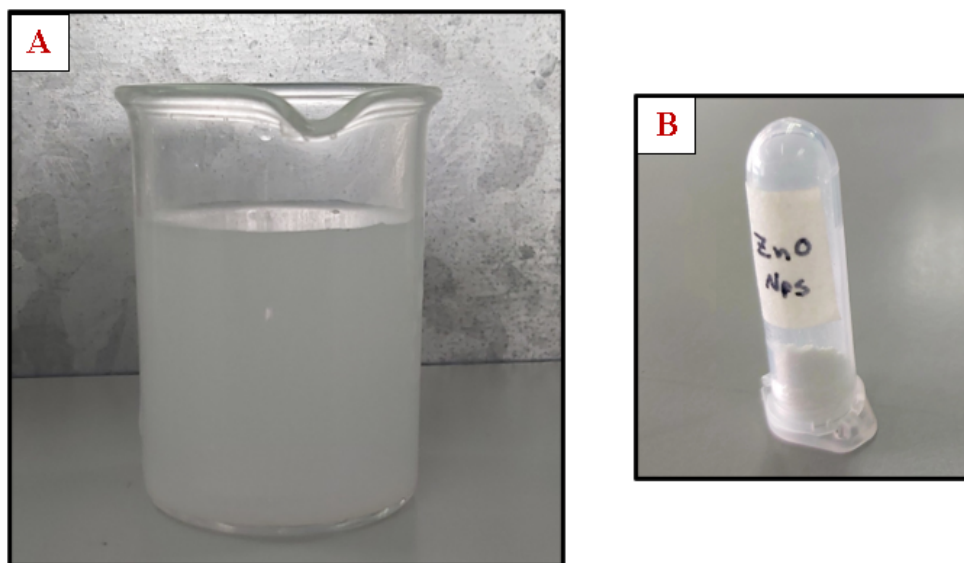


Figure 4.3: Results of the ZnO nanoparticles synthesis with A) The solution obtained from the synthesis and B) the ZnO powder obtained after the calcination process.

Visual analysis of the ZnO nanoparticle suspension before centrifugation revealed minimal precipitate formation at the base of the Erlenmeyer flask, as shown in Figure 4.3A. This observation is consistent with the synthesis procedure, which was optimized for a low nanoparticle yield, suitable for the scale of composite film production required in this study. The transparency of the supernatant liquid suggests successful dispersion of the ZnO particles, a critical factor in achieving particle size uniformity after centrifugation.

After centrifugation and drying, the ZnO nanoparticles formed a fine white powder, as seen in Figure 4.3B. The amount obtained was remarkably lower than TiO₂ nanoparticles, underlining the controlled synthesis process tailored to produce smaller batches. Despite the lower yield, the quality of the ZnO powder did not appear to be compromised. The homogeneity of the powder suggests that it will exhibit consistent properties when integrated into the chitosan matrix, which is critical for investigating the photoconductivity of the composite.

4.4 UV-Vis Spectroscopy Characterization

The UV-Vis spectra depict TiO₂'s and ZnO's (NPs) optical properties in figure 4.4. The reflectance spectrum shows the wavelength at which the reflectance starts to increase sharply, indicating the absorption edge of the nanoparticles. TiO₂ nanoparticles' reflectance edge occurs at a lower wavelength than ZnO nanoparticles, suggesting a higher band gap for TiO₂. The Tauc plot, a graphical representation used to determine the optical band gap of semiconductors, corroborates this in figure 4.5. The band gap energies calculated from the Tauc plots are 3.25 eV for TiO₂ nanoparticles and 3.17 eV for ZnO nanoparticles.

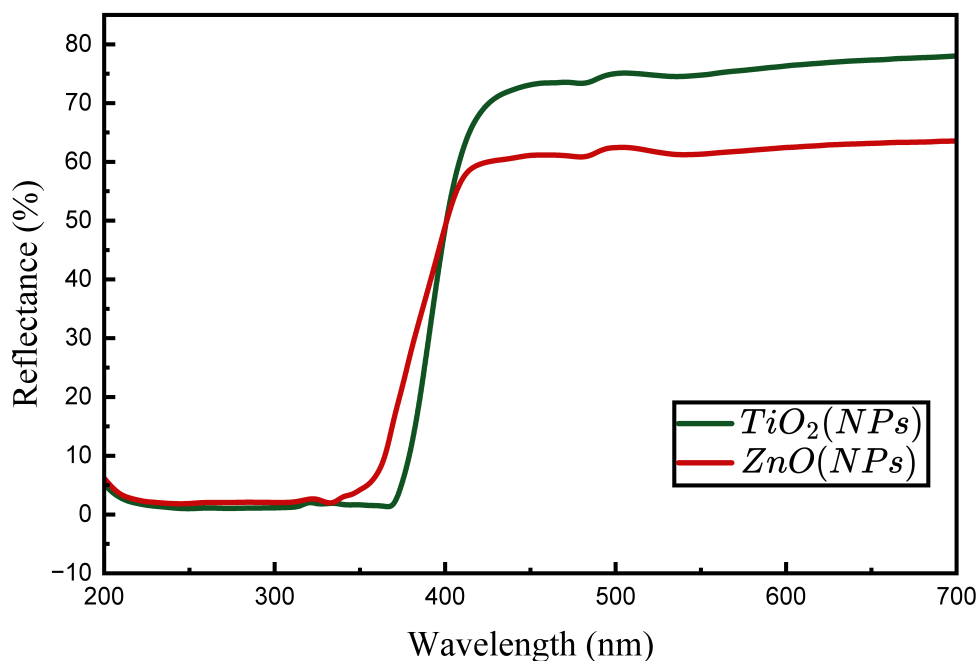


Figure 4.4: Optical Reflectance (%R) obtained of TiO₂ and ZnO NPs.

The band gap values are characteristic of these materials and are influenced by the size of the nanoparticles. Generally, as the size of semiconductor nanoparticles decreases, quantum confinement effects can increase the band gap¹⁹. The obtained values are within the expected range for these materials and suggest that both types of nanoparticles have sufficiently small sizes to exhibit these effects.

TiO₂ nanoparticles typically have a band gap in the range of 3.2 eV to 3.35 eV, depending on the crystalline phase and particle size¹⁹. The observed band gap of 3.25 eV suggests that the TiO₂ nanoparticles are likely in the anatase phase.

ZnO nanoparticles exhibit a band gap around 3.10 eV to 3.37 eV, which aligns with the measured value of 3.17 eV. ZnO is known for its wide band gap and exciton binding energy. The slightly higher band gap found in ZnO nanoparticles suggests either a smaller particle size or a higher degree of crystallinity, which is desirable

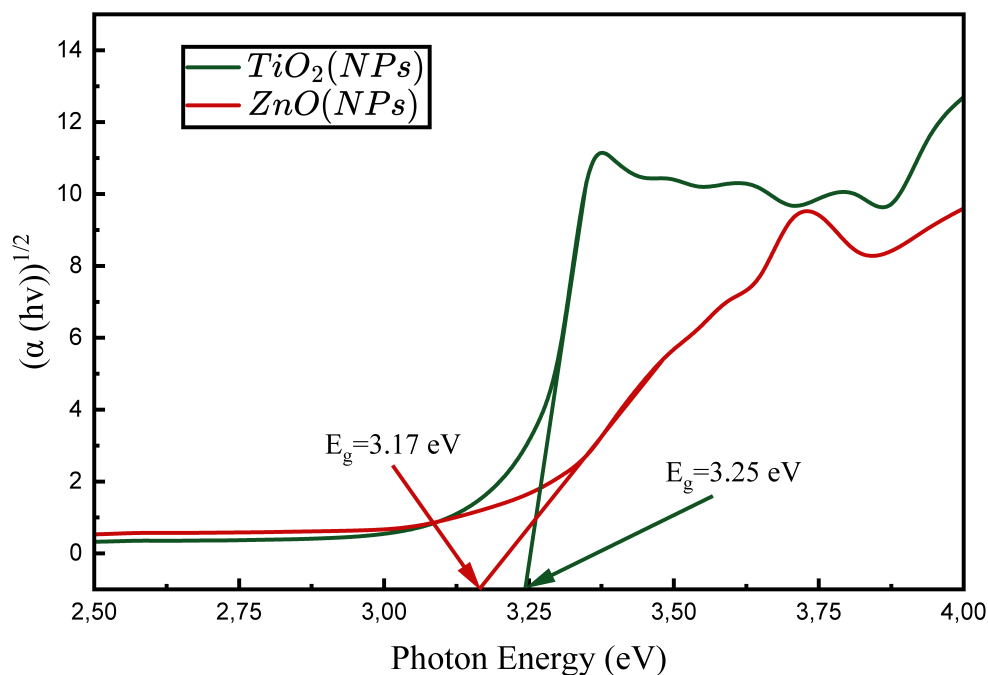


Figure 4.5: Tauc plot obtained to find the band gap of TiO_2 and ZnO NPs.

for applications in optoelectronics and as UV blockers in sunscreens due to their ability to absorb and reflect UV radiation⁵⁸.

Both materials show sharp increases in their reflectance spectra at wavelengths corresponding to their band edges, indicative of strong absorption and efficient photoactivity within the UV region. These properties are particularly important for photocatalytic applications where generating electron-hole pairs is crucial for the reaction processes⁵⁹. The optical characterization of TiO_2 and ZnO nanoparticles through UV-Vis reflectance spectroscopy and Tauc plots reveals distinct band gaps indicative of their semiconductor properties. The results are consistent with the literature, suggesting that these nanoparticles can be effectively utilized in applications that exploit their optical properties, in this case, for photoconductance.

4.5 Powder X-Ray Diffraction (XRD) Characterization

The X-ray diffraction (XRD) analysis of the synthesized titanium dioxide (TiO_2) nanoparticles is presented in Figure 4.6. The diffraction pattern exhibits prominent peaks corresponding to the (101), (103), (004), (112), (200), (105), (211), (204), (116), (220), (215), and (224) planes, which are indicative of the anatase crystal structure of TiO_2 . This phase is often the most stable at room temperature and is commonly observed in TiO_2 nanoparticles. These peaks' well-defined and symmetric nature suggests a high degree of crystallinity within the nanoparticle sample.

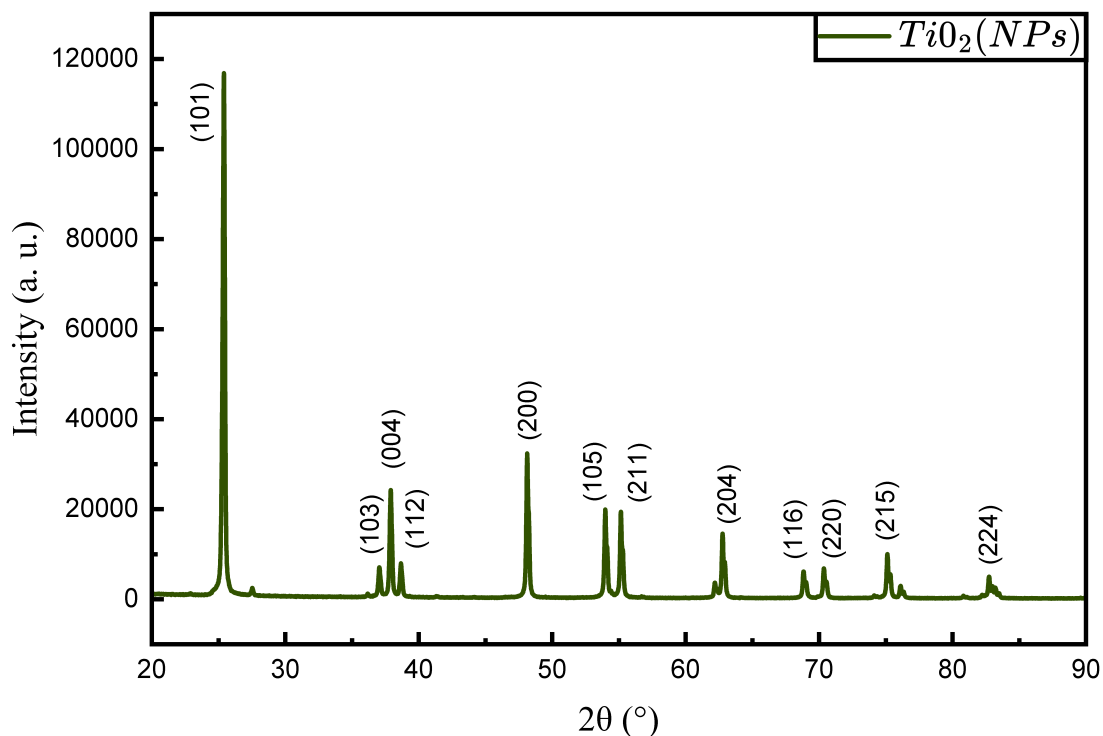


Figure 4.6: XRD pattern of TiO_2 nanoparticles.

Significantly, the absence of additional peaks not associated with the anatase phase implies the high purity of the nanoparticles, with no detectable presence of rutile or other impurities. Anatase TiO_2 is recognized for its applications in photovoltaic cells, photocatalysts, and antimicrobial properties. Its crystal structures, such as anatase, rutile, and brookite, impact its performance in these applications Hariharan et al.⁶⁰. The average crystallite size was calculated to be approximately 50 nm using the Scherrer equation on the broadening of these peaks. This size is substantial for nanoparticles and could have important implications for their application, as it strikes a balance between the reactivity of smaller nanoparticles and the stability of larger bulk structures. The potential for TiO_2 nanomaterials in applications beyond photocatalysis, such as in batteries, sensors, and catalysts, is also significant. Anatase TiO_2 , due to their unique structure, has shown potential for applications in photovoltaic cells, batteries, sensors, and catalysts, with their transport properties being a key factor Kim et al.⁶¹. The anatase phase, in particular, is known for its photocatalytic efficiency under UV light. A crystallite size of 50 nm indicates that the nanoparticles have a significant surface area, enhancing their photocatalytic activity. This size may also influence the dye-sensitization process, making these nanoparticles suitable for use in dye-sensitized solar cells, as larger crystallite sizes can facilitate the absorption of dyes and improve charge separation efficiency.

The X-ray diffraction (XRD) patterns of the synthesized ZnO nanoparticles are shown in Figure 4.7. The

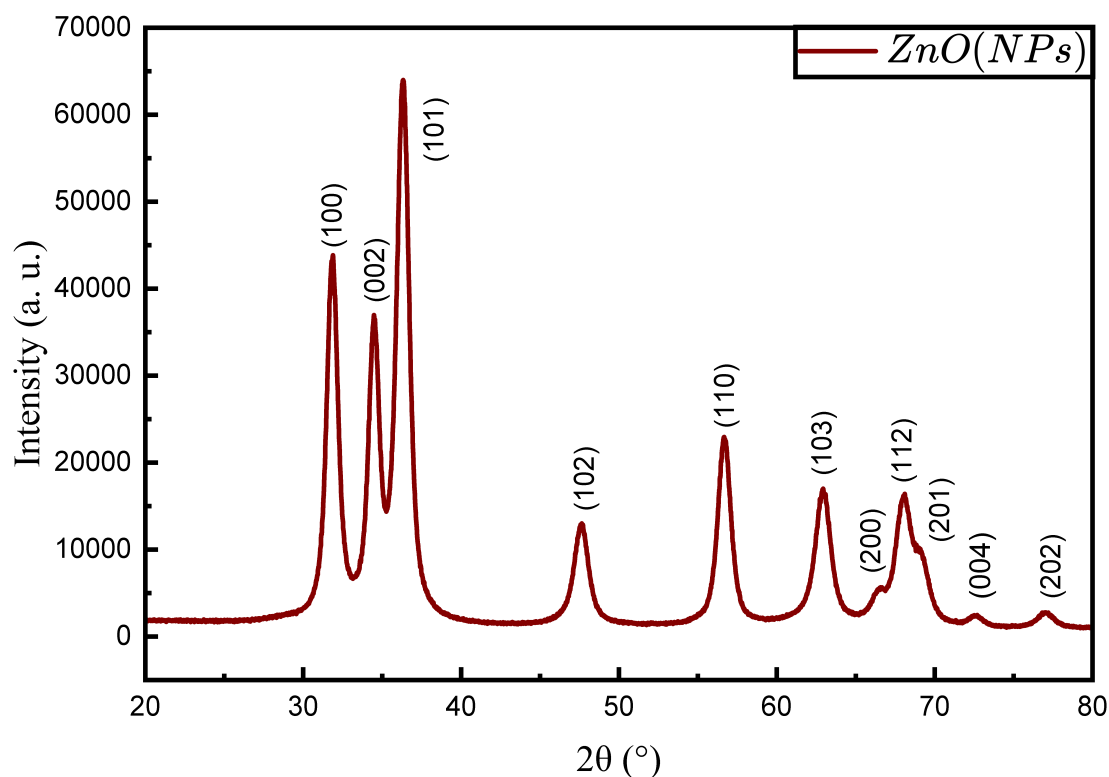


Figure 4.7: XRD pattern of ZnO nanoparticles.

prominent peaks observed at 2θ correspond to the (100), (002), (101), (102), (110), (103), (200), (112), (201), (004), and (202) planes, indicative of the wurtzite crystal structure of ZnO, by the reference patterns of the Joint Committee on Powder Diffraction Standards (JCPDS). The absence of additional peaks suggests that the nanoparticles are of high purity and do not contain significant secondary phases. Applying the Scherrer equation to the diffraction peaks yielded an average crystallite size of approximately 11 nm. The characterization of the ZnO nanoparticles through X-ray diffraction revealed patterns consistent with the wurtzite crystal structure, in concordance with the findings of Bouazizi et al.⁶⁰, who also observed a wurtzite crystal structure in ZnO nanoparticles. The synthesis methodology employed here appears to influence the reduction in crystallite size compared to the methods used by Franco and Pessoni⁶², who reported crystallite sizes of approximately 16 nm for ZnO samples. These results suggest that optimizing synthesis conditions could be crucial for controlling the dimensions of ZnO nanoparticles, essential for their applications in optoelectronic devices, which are particularly interesting for photovoltaic applications, notably influenced by the size of the nanoparticles. Manikandan et al.⁶³ highlighted that ZnO nanostructures with crystallite sizes ranging from 10 to 28 nm are suitable for dye-sensitized solar cells. Therefore, as reported in this study, ZnO nanoparticles with a crystallite size of 11 nm could exhibit improved performance due to a larger surface-to-volume ratio, potentially enhancing interaction with dyes and efficiency in charge separation.

4.6 Dynamic Light Scattering (DLS) Characterization

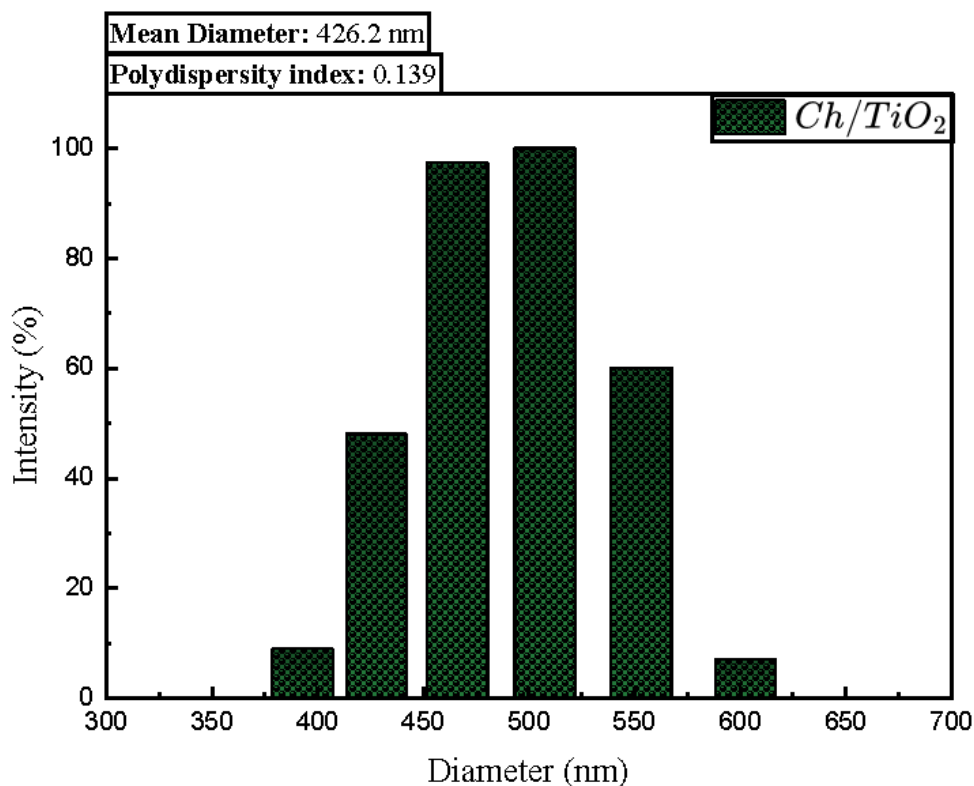


Figure 4.8: DLS measurement to determine the size distribution of TiO₂ NPs in the chitosan matrix.

Dynamic Light Scattering (DLS) is a widely used method for determining the size distribution of particles in a suspension. In the case of Ch/TiO₂ nanoparticles, the DLS results indicate a mean diameter of 426.2 nm with a polydispersity index of 0.139, as shown in Figure 4.8. The polydispersity index is a dimensionless number indicating the broadness of size distribution within the sample; a value close to 0 indicates a very monodisperse distribution, while values closer to 0.5 suggest a broad size distribution. The relatively low polydispersity index observed here suggests a fairly uniform size distribution of nanoparticles. The intensity distribution shows that most particles have a diameter in the 450-500 nm range, as evidenced by the highest intensity peak indicating the presence of larger particles or particle aggregates.

The DLS results indicate a mean diameter of 297.3 nm for Ch/ZnO nanoparticles, with a notably low polydispersity index (PDI) of 0.059, shown in Figure 4.9. This low PDI value suggests that the particle size distribution is very narrow, implying a uniform nanoparticle size within the sample. The relatively low polydispersity index observed here suggests a fairly uniform size distribution of nanoparticles. The intensity distribution shows that most particles have a diameter in the 297-305 nm range, as evidenced by the highest intensity peak indicating the presence of larger

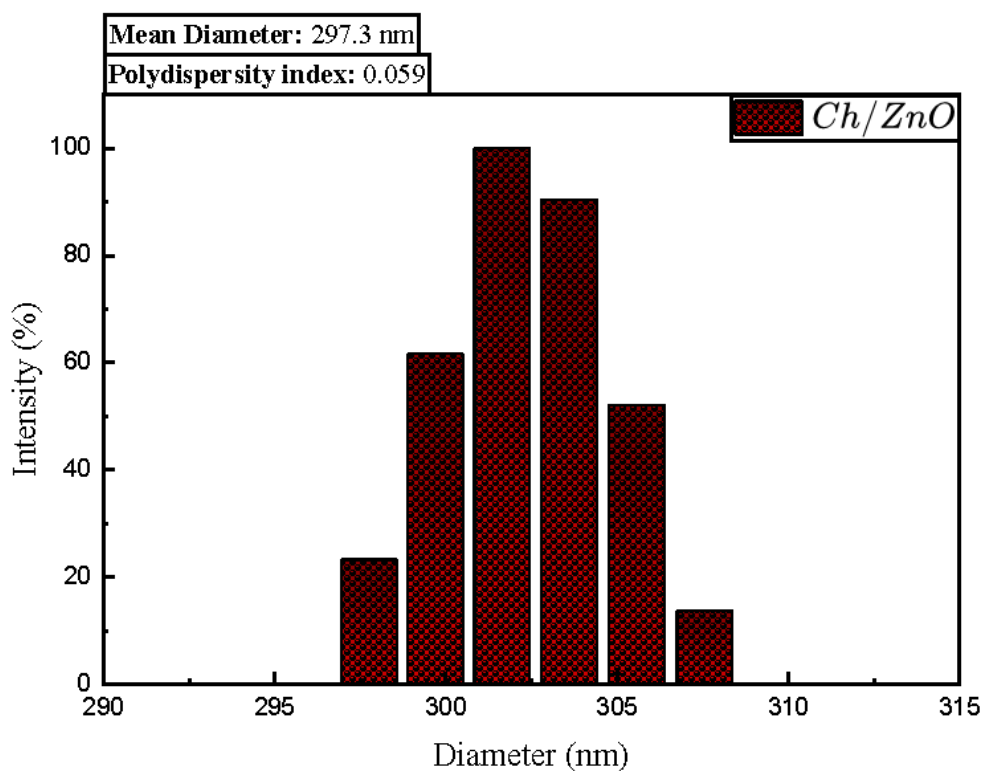


Figure 4.9: DLS measurement to determine the size distribution of ZnO NPs in the chitosan matrix.

particles or particle aggregates.

The larger size observed through DLS compared to other characterization methods, which suggests a size range of much less, may be attributed to several factors. DLS measures the hydrodynamic diameter of particles, including the core particle, any attached molecules, and the solvation layer, leading to a larger apparent size. Aggregation and sedimentation behaviors in the suspension can also affect the DLS measurement, often resulting in an increased apparent size due to the detection of agglomerates rather than individual nanoparticles.

Another reason for the discrepancy might be the optical properties of the nanoparticles and the medium in which they are suspended. Nanoparticles with high refractive index differences compared to the surrounding medium can scatter light more efficiently, which the DLS instrument might interpret as a larger size⁶⁴. Furthermore, sample preparation and the presence of surfactants or other stabilizing agents in the DLS measurement can stabilize larger aggregates, which can increase the measured size. These agents can affect the zeta potential and the stability of the nanoparticles, preventing them from settling or aggregating, which would normally reduce the measured size⁶⁵.

4.7 Atomic Force Microscopy (AFM) Characterization

The Atomic Force Microscopy (AFM) analysis of the Ch/TiO₂, Ch/ZnO and Ch/TiO₂/ZnO composites was conducted to examine the surface morphology and nanoparticle size distribution. The images obtained from the AFM provide both two-dimensional (2D) and three-dimensional (3D) representations of the sample surface.

First, we have a detailed examination of the surface topography of the Ch/TiO₂ composites. The 2D AFM image in Figure 4.10a, a topographic map, reveals variations in height through the colors where darker regions correspond to lower elevations on the sample surface, and lighter regions indicate higher elevations, typically associated with greater nanoparticles. The scale of the image ranges from 0 to 84 nm. From the analysis of this image, it is evident that most of the nanoparticles are within the size range of 20 to 40 nm. This suggests a relatively uniform distribution of nanoparticles across the surface with a moderate degree of aggregation.

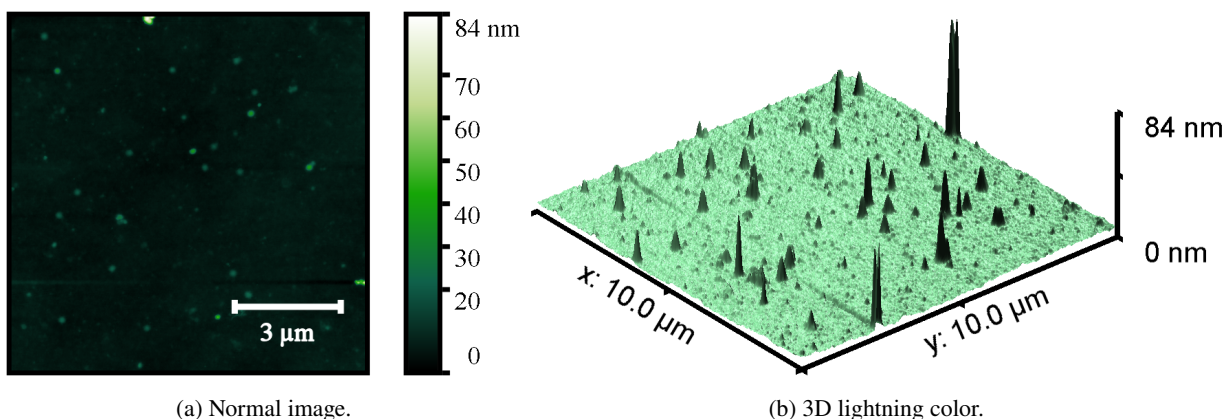


Figure 4.10: AFM analysis images for the morphology of Ch/TiO₂. The normal and the 3D image by applying lightning color.

The 3D processed AFM image in Figure 4.10b offers a different perspective, emphasizing the topographical variation of the sample. Peaks and valleys are clearly distinguished, providing a visual representation of the surface's roughness. The 3D AFM image, processed with lightning color to enhance the topographic features, provides a more intuitive visualization of the sample's surface texture. The pronounced peaks and valleys highlight the distribution and height of the nanoparticles on the Chitosan matrix. The height of these features is consistent with the measurements obtained from the 2D representation, confirming the presence of nanoparticles in the 20 to 40 nm range.

As indicated by both AFM images, the uniformity in nanoparticle size indicates a well-controlled synthesis process for the Ch/TiO₂ composite. The observed nanoparticle size range is crucial for the application required in this research.

The 2D AFM image for the Ch/ZnO composite in Figure 4.14 showcases the surface topology through a color gradient, with darker areas representing the lower surface features and lighter areas indicating higher features, typically the nanoparticles. The scale on this image indicates that the height variation spans from 0 to 32 nm.

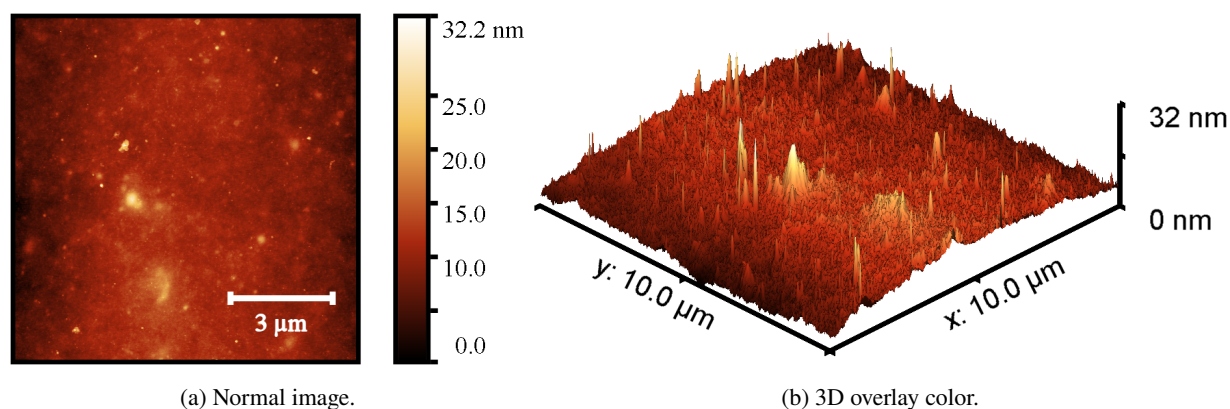


Figure 4.11: AFM analysis images for the morphology of Ch/ZnO. The normal and the 3D image by applying overlay color.

Compared to the Ch/TiO₂ composite, this relatively smaller range could suggest a smoother surface or a more uniform particle distribution within the size constraints.

The 3D AFM image in Figure 4.14b is rendered with color gradients to accentuate the topography, giving a vivid depiction of the surface's peaks and valleys. In this Ch/ZnO composite, the 3D visualization aids in assessing the physical dispersion of the nanoparticles and provides a qualitative sense of their spatial arrangement on the substrate. The peaks, corresponding to the lighter areas in the 2D image, show that distinct nanoparticles protrude above the chitosan matrix, with heights reaching up to 32 nm.

Comparing both composites, the Ch/ZnO appears to have a less extensive range of particle sizes and possibly a more homogeneous nanoparticle distribution. The size of nanoparticles, as with the Ch/TiO₂, is significant as it impacts the composite's properties and potential application.

The AFM analysis of the Ch/TiO₂/ZnO composite reveals a significant finding regarding the size of the nanoparticles within the material. The 2D AFM image in Figure 4.12a) demonstrates that the composite possesses the largest nanoparticles among the analyzed samples, predominantly between 100 and 200 nm (0.1 to 0.2 μm), notably larger than those observed in the Ch/TiO₂ and Ch/ZnO composites. This observation is further supported by the 3D AFM image in Figure 4.12b), where the peaks corresponding to these nanoparticles are distinctly taller than those in the other composites.

Most of the nanoparticles within the Ch/TiO₂/ZnO composite are observed to be between 30 and 50 nm, suggesting a bimodal distribution with a significant quantity of smaller nanoparticles and a notable presence of much larger ones. This bimodal distribution may indicate different mechanisms at play during the formation or aggregation of the nanoparticles within the chitosan matrix.

There could be several factors for this interesting occurrence. Among them is that when TiO₂ and ZnO nanoparticles are combined within a chitosan matrix, the synergistic effect between these two types of nanoparticles can lead to a higher degree of particle agglomeration. This agglomeration process results in the formation of larger

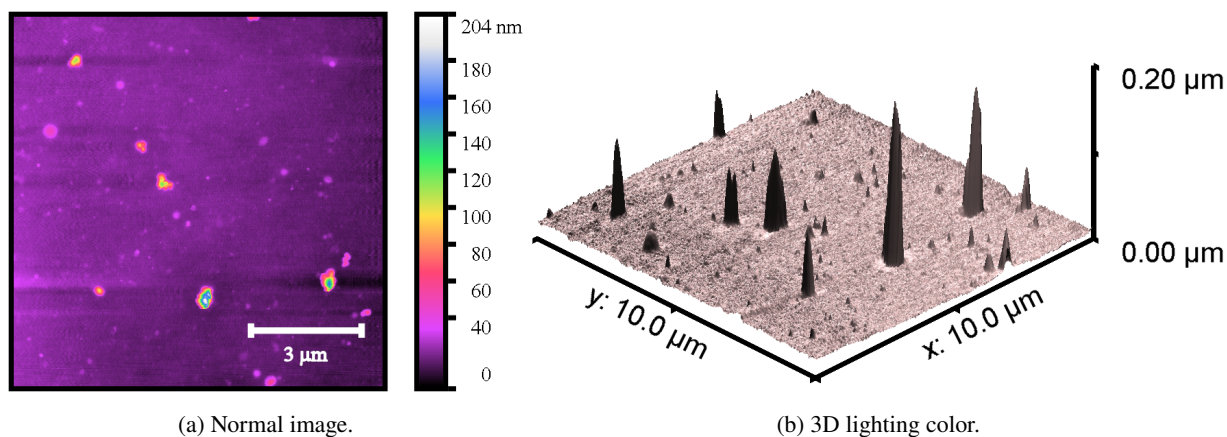


Figure 4.12: AFM analysis images for the morphology of Ch/TiO₂/ZnO. The normal and the 3D image by applying lightning color.

composite particles. Both types of nanoparticles can increase the likelihood of particle-particle interactions, forming larger aggregates than individual nanoparticles dispersed in the matrix separately⁶⁶.

Also, the chemical interactions between TiO₂ and ZnO nanoparticles with chitosan could differ when combined compared to when added separately. Chitosan, a natural polymer with functional groups capable of interacting with metal oxide nanoparticles, can stabilize these nanoparticles to varying degrees. When both types of nanoparticles are present, the interaction dynamics change, which can result in more stable and, thus, larger agglomerates due to increased cross-linking or binding within the matrix⁶⁷.

4.8 Sonication dispersion of nanoparticles in the chitosan solution

Figure 4.13 presents the sonicated solutions of the chitosan composites, each with 0.7% w/v nanoparticle concentration. The beakers are labeled CH/TiO₂, CH/ZnO and CH/TiO₂/ZnO, visually comparing the solutions after the sonication process.

The CH/TiO₂ solution is homogeneous and opaque, suggesting a uniform distribution of TiO₂ nanoparticles within the chitosan matrix. TiO₂ nanoparticles exhibit strong scattering and reflection properties due to their high refractive index and the presence of a broad bandgap. Thus, when TiO₂ nanoparticles are dispersed in a chitosan solution, the solution usually appears white because TiO₂ scatters visible light very effectively. This effect is enhanced in the presence of chitosan, which can help to disperse the TiO₂ nanoparticles evenly, increasing the scattering effect throughout the visible spectrum and making the solution appear white⁶⁸. This uniformity is essential to achieve consistent photoconductive properties in the composite films. In contrast, the CH/ZnO solution appears significantly more transparent due to the different physical or chemical interactions between the ZnO nanoparticles and the chitosan matrix. These also have a wide bandgap but can be synthesized to form structures that minimize

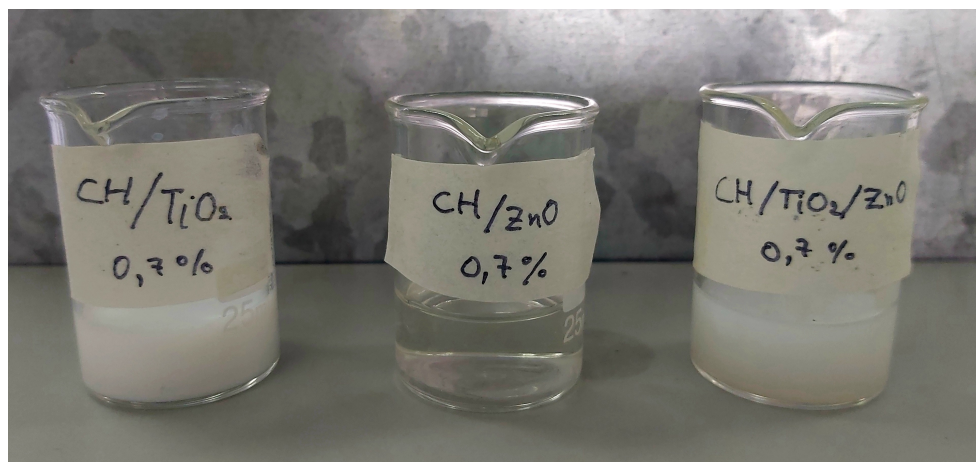


Figure 4.13: Each of the solutions obtained after the sonication process. Each at 0.7% w/v.

scattering and absorption of visible light, especially when well-dispersed in a matrix like chitosan. Chitosan can act as a stabilizing agent, preventing agglomeration of ZnO nanoparticles and allowing for a more uniform distribution that can lead to the solution's transparent or semi-transparent appearance. The transparency in the chitosan-ZnO solutions can also be attributed to the smaller size of ZnO nanoparticles, which can reduce the scattering of light, making the solution appear clear⁶⁹.

Interestingly, the CH/TiO₂/ZnO solution has a very similar appearance to the CH/TiO₂ solution, suggesting that the presence of ZnO nanoparticles does not drastically alter the visual consistency of the composite. This could indicate that the sonication process effectively achieved fine dispersion of the TiO₂ and ZnO nanoparticles within the chitosan matrix.



Figure 4.14: Gelation of the Ch/ZnO solution by not adding 20% acetic acid.

In the case that we do not add the 20% acetic acid, there is the formation of a gel when sonicating the Ch/ZnO and Ch/TiO₂/ZnO solution, and this can be attributed to several factors influenced by the sol-gel process and the specific conditions under which sonication is performed. When a solution begins to heat up during sonication, the temperature increase can accelerate the hydrolysis and condensation reactions of the metal precursors, forming a gel-like structure. This process is part of the sol-gel method, which commonly happens in the synthesis of metal oxides such as ZnO. Gel formation indicates the transition from a colloidal solution (sol) to a semi-solid state (gel), characterized by the formation of networks of metal oxide particles⁷⁰.

Adding 20% acetic acid to the solution is likely to aid homogenization by affecting the pH and surface charge of the particles, which may influence the dispersion and stability of the particles in the solution. Acetic acid, being a weak acid, can protonate the surface hydroxyl groups of the ZnO particles, reducing the surface charge and thus decreasing the electrostatic repulsion between the particles. This can result in a better dispersed and more stable colloidal system, preventing premature gelling and aggregation of the particles. In addition, acetic acid acts as a complexing agent, binding to the zinc ions and controlling the release of these ions into solution, which further helps to control the dispersion and morphology of the ZnO particles, resulting in a more uniform and homogenized solution after sonication⁷¹.

4.9 Films fabricated on interdigitated electrodes



Figure 4.15: Composite added to the interdigitate for the drying process, each one delimited. Ch/TiO₂, Ch/ZnO, Ch/TiO₂/ZnO respectively.

Figure 4.15 illustrates the crucial film deposition stage for Ch/TiO₂, Ch/ZnO, and Ch/TiO₂/ZnO solutions on interdigitated electrodes. Figure 4.16 further reveals the appearance of the resultant films. The uniformity and consistency observed in these images are promising, indicating a successful transition from liquid composites to solid-state films.

A noteworthy observation during the drying process, especially for the Ch/TiO₂ and Ch/TiO₂/ZnO films, was the critical sensitivity to the duration of exposure to the drying environment. Exceeding the drying time specified in the methodology could lead to the degradation or detachment of the TiO₂ containing films from the interdigitate

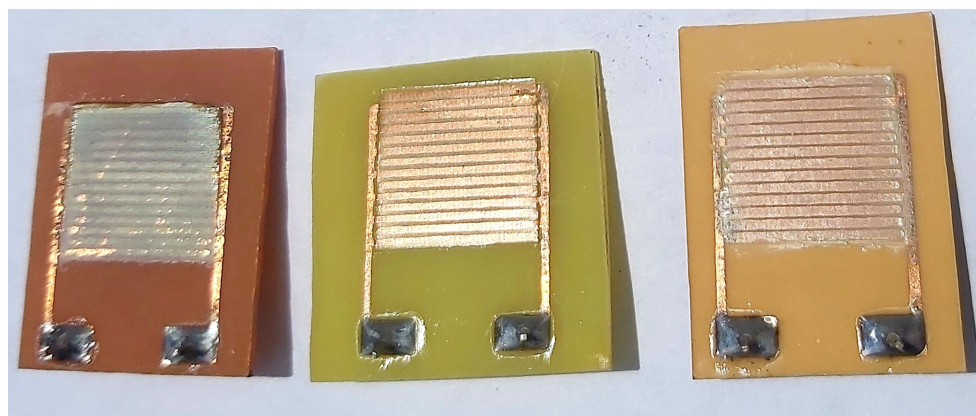


Figure 4.16: Films created after the drying stage. Ch/TiO₂, Ch/ZnO, Ch/TiO₂/ZnO respectively.

substrates. This susceptibility is likely due to the photocatalytic activity of TiO₂, which could lead to the degradation of the chitosan matrix under prolonged exposure to light and air. Meticulous adherence to the drying protocol is, therefore, essential to preserve the integrity of the films.

Despite these challenges, the final films exhibited remarkable consistency and uniformity. As seen in the images in Figure 4.16, the absence of cracking or peeling in the final film products suggests that the drying process was well-optimized for the Ch/ZnO films, which displayed less opacity and potential for higher light transmittance. On the other hand, the TiO₂-containing films, while more robust, required careful handling to prevent photo-induced degradation.

The Ch/TiO₂ films demonstrated the expected opaque quality, while the Ch/ZnO films maintained a semi-translucent appearance. Interestingly, the Ch/TiO₂/ZnO composite films achieved a homogenous blend of these characteristics, suggesting that the combination of nanoparticles did not compromise film integrity. The uniformity of these films, confirmed through visual inspection, indicates a successful sonication and substrate application process.

4.10 Photoconductivity of Ch/TiO₂ Composite Films

The photoconductivity measurements of Ch/TiO₂ composite films with varying concentrations of TiO₂ exhibit distinct behaviors under cycles of UV light exposure as shown in Figure 4.17. These variations in electrical response highlight the influence of TiO₂ concentration on the photoactive properties of the films. The difference in the behavior of films with different concentrations of TiO₂ could be attributed to a combination of factors, including the efficiency in charge carrier generation, the density and distribution of recombination sites, and the interaction between TiO₂ and the chitosan matrix. At lower concentrations, TiO₂ may not form a continuous network sufficient for effective charge transfer, while higher concentrations provide a form a good mott conduction that facilitates the transport of electrons and holes.

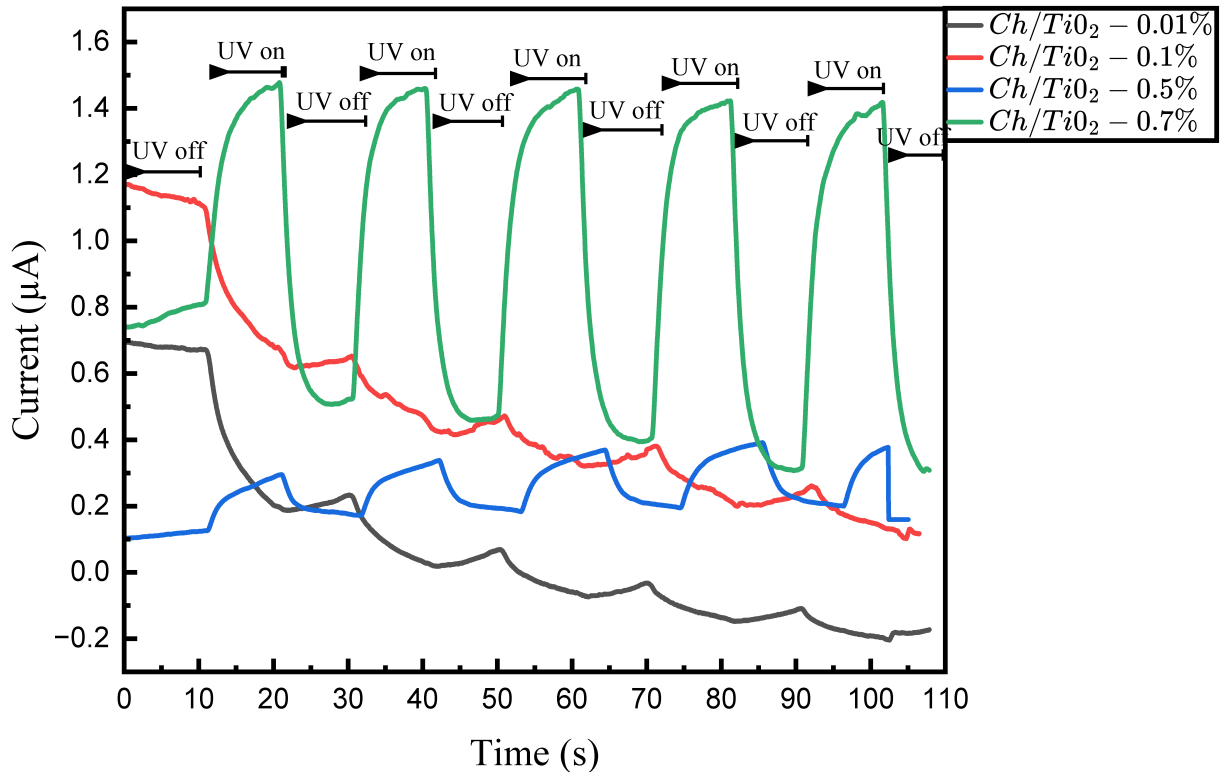


Figure 4.17: Rise and fall curves of Ch/TiO₂ depending on exposure and non-exposure to UV light (all concentrations).

4.10.1 Effects of the assigned TiO₂ concentrations

The films with 0.01% (black curve) and 0.1% (red curve) TiO₂ concentrations in Figure 4.18 exhibit a decrease in current upon UV illumination, which is typical for photoconductive materials. This behavior suggests the predominance of processes that limit charge carrier mobility, such as recombination or trapping. The films may be experiencing an increase in recombination centers or a surface effect that impedes the charge separation process^{72,73}.

The ability of the films to return to their low conductivity state upon turning off UV light indicates good photoconductivity reversibility. We can observe in Figure 4.19 that the film with 0.5% TiO₂ appears to exhibit the highest reversibility and the most stable response, which could be an indication of an optimal balance between charge generation and recombination at this concentration. Doping TiO₂ with various elements in this case chitosan can create mid-gap states that facilitate charge carrier separation and enhance photocatalytic activity under visible light⁷⁴. While the film with 0.7% TiO₂ (green curve) shows the highest current under UV illumination, it also exhibits a higher residual current when UV light is turned off. This may indicate a higher rate of charge carrier recombination in the dark, which could reduce the material's efficiency in rapid light cycling applications.

This enhanced photoconductivity points to a more effective separation of electron-hole pairs and suggests that

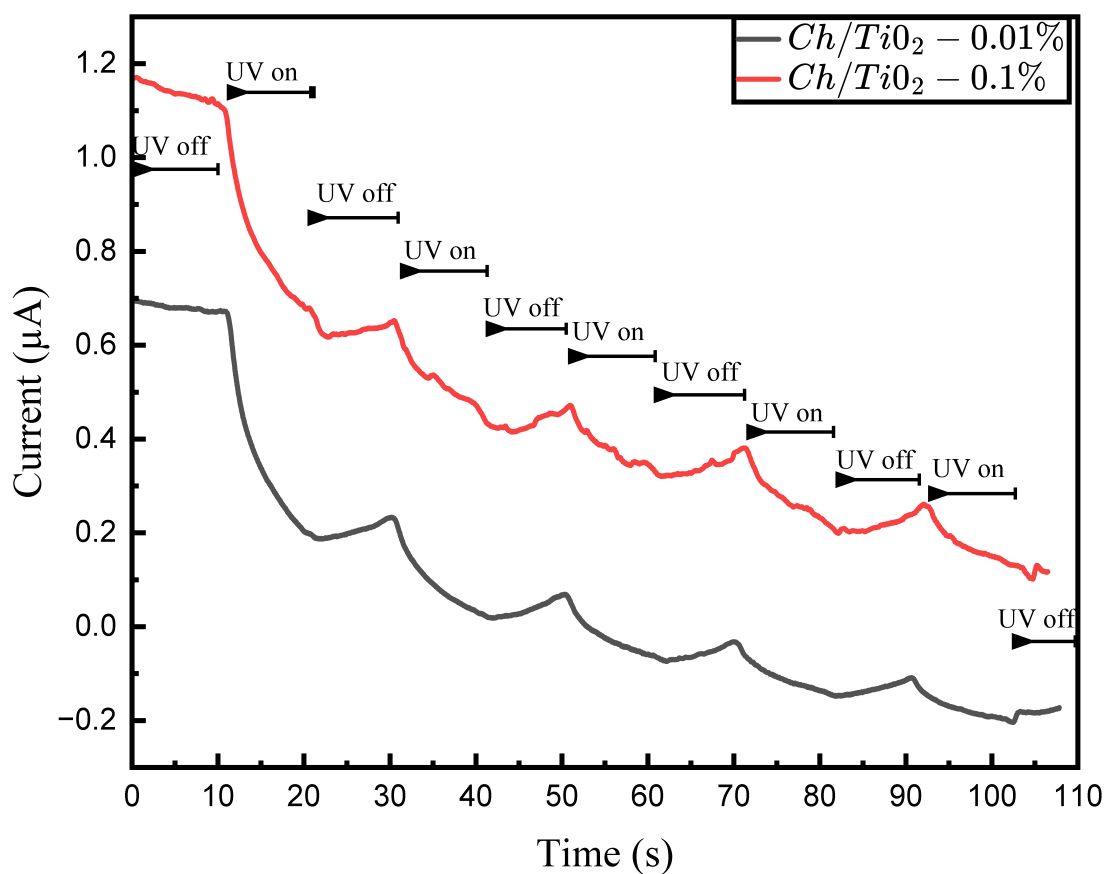


Figure 4.18: Rise and fall curves of Ch/TiO₂ depending on exposure and non-exposure to UV light(0.01 and 0.1).

these concentrations of TiO₂ within the chitosan matrix form a good mott conduction to electron transport. This concept within nanocomposites involves creating pathways through which electrons can move more efficiently, thus enhancing the material's conductivity. In this context, the TiO₂ nanoparticles can act as conductive nodes within the insulating chitosan matrix, forming a network that facilitates electron transport. This arrangement can improve electron-hole pairs' separation and transport to the surface, where photocatalytic reactions occur⁷⁵.

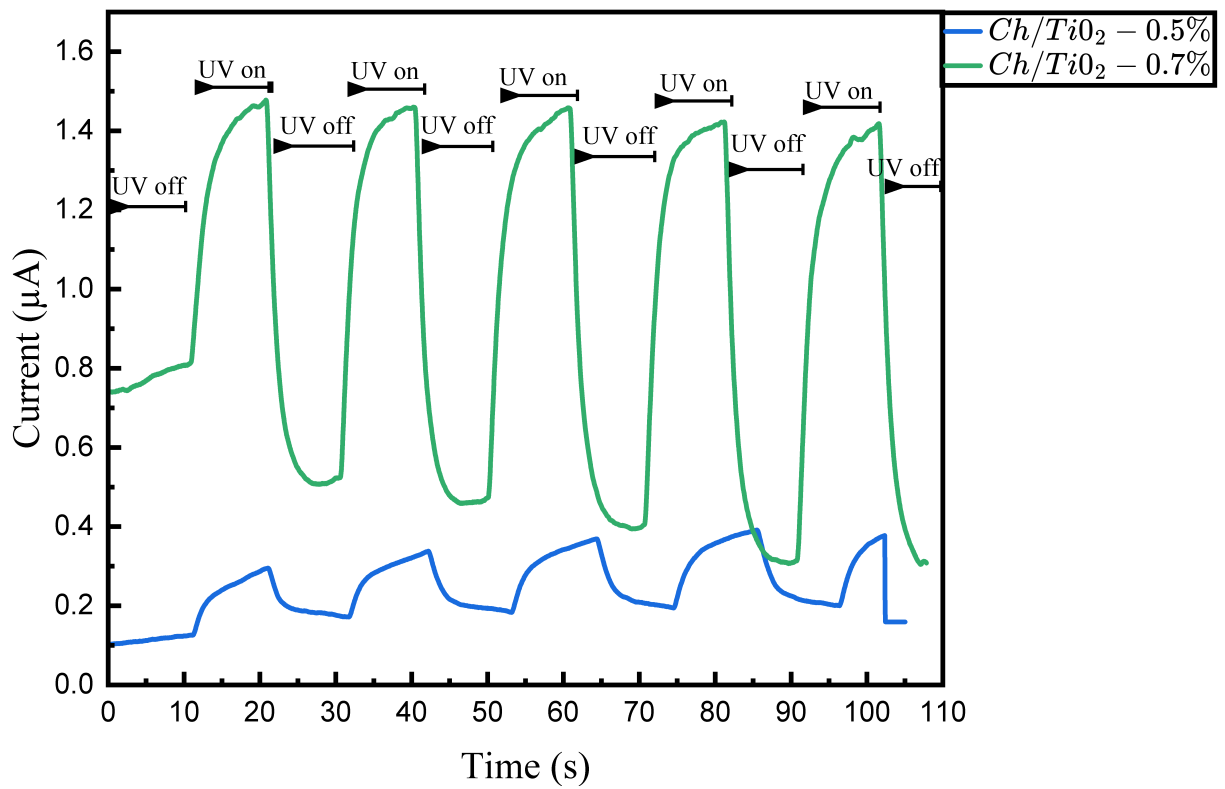


Figure 4.19: Rise and fall curves of Ch/TiO₂ depending on exposure and non-exposure to UV light(0.5 and 0.7).

4.11 Photoconductivity of Ch/ZnO Composite Films

4.11.1 Effects of the assigned ZnO concentrations

Photoconductivity measurements of Ch/ZnO composite films have been performed under UV light exposure to understand the influence of ZnO nanoparticle concentration on the electrical behavior of the films. The general photoconductivity of Ch/ZnO films exhibits different photoconductivity behaviors depending on the concentration of ZnO.

Films with low concentrations of ZnO (0.01% and 0.1%) in Figure 4.20 experience a decrease in current when exposed to UV light, which could be interpreted as a negative photoconductivity effect or an enhanced efficiency in charge carrier recombination processes under UV light. On the other hand, films with higher concentrations do not exhibit this behavior, suggesting that higher concentrations of ZnO may promote charge carrier generation and, consequently, increase conductivity under UV illumination.

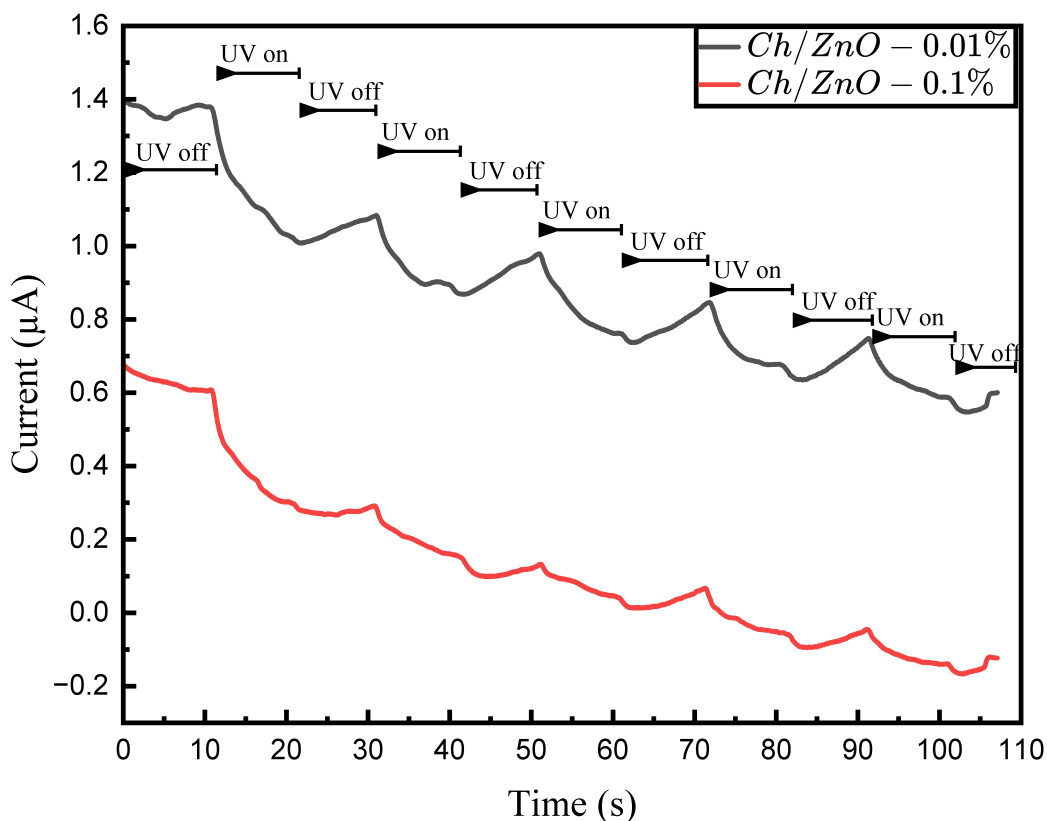


Figure 4.20: Rise and fall curves of Ch/ZnO depending on exposure and non-exposure to UV light(0.01 and 0.1).

Interestingly, the films with 0.5% and 0.7% ZnO concentrations in Figure 4.21 show imperceptible changes in

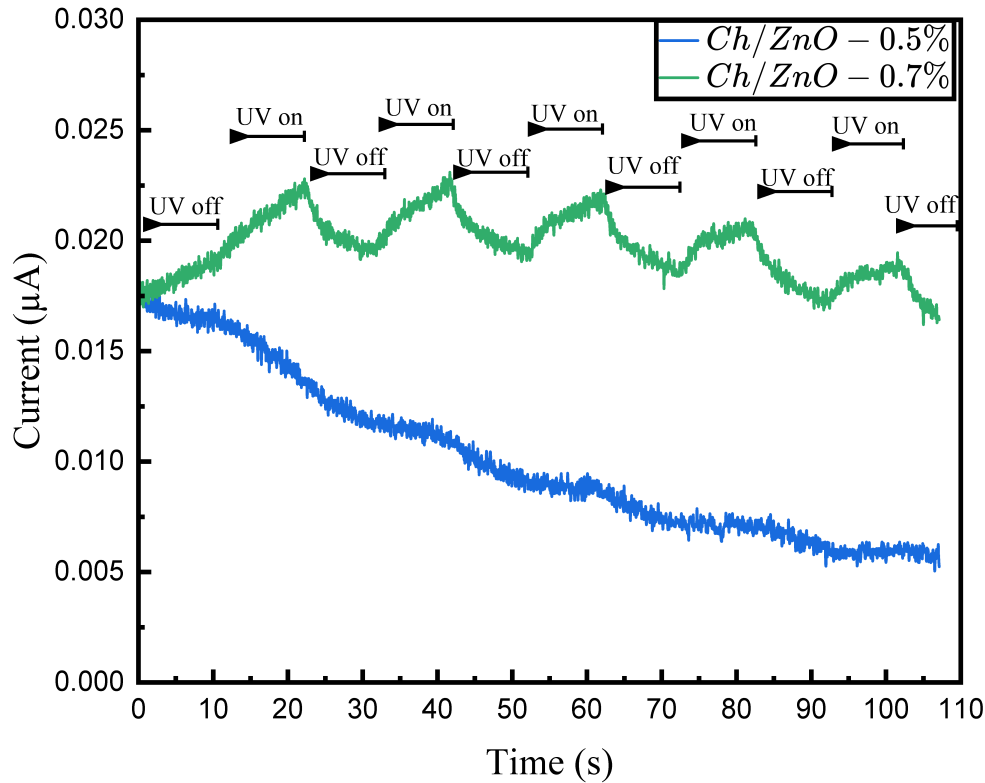


Figure 4.21: Rise and fall curves of Ch/ZnO depending on exposure and non-exposure to UV light(0.5 and 0.7).

photocurrent under UV light exposure. This could be due to a saturation effect where the density of ZnO nanoparticles is high enough that additional light does not significantly change the number of charge carriers or their mobility.

Alternatively, the interface between ZnO nanoparticles and the chitosan matrix may play a role in charge carrier dynamics that needs further investigation. ZnO nanoparticles can introduce deep traps within a Chitosan matrix, likely to scatter charge carriers and potentially inhibit the conductance current. Also, the mobility of charge carriers tends to be responsible for hopping and electronic polarization. This could imply that within a Chitosan matrix, ZnO nanoparticles may affect the dielectric constant and conductance current⁷⁶.

Increasing the electric field strength while introducing nanoparticles into a solution results in a suppressive impact on the conductance current. Increased filler content enhances the inhibitory effect due to the introduction of nanoparticles into the chitosan, which creates deep traps and scatter charge carriers. The microparticles enhance the current conductance in direct relation to the amount of filler present, G Yu et al. (2022) reported that a 5% inhibitory effect has the largest impact on charge carriers' mobility, while a 10% promotional effect has the highest impact on carriers' mobility⁷⁷.

4.12 Photoconductivity of Ch/TiO₂/ZnO Composite films

This section details the photoconductivity responses of chitosan-based composite films with TiO₂ and ZnO nanoparticles (Ch/TiO₂/ZnO) under intermittent UV light exposure. The overall behavior observed from the composite films in Figure 4.22 suggests that the photoconductivity is highly dependent on the nanoparticle concentration. Lower concentrations of nanoparticles tend to decrease in current upon UV exposure, hinting at possible charge trapping or enhanced recombination mechanisms. Higher nanoparticle concentrations generally exhibit an increase in photocurrent with UV light, indicative of effective charge carrier generation.

4.12.1 Effects of the assigned TiO₂/ZnO concentrations

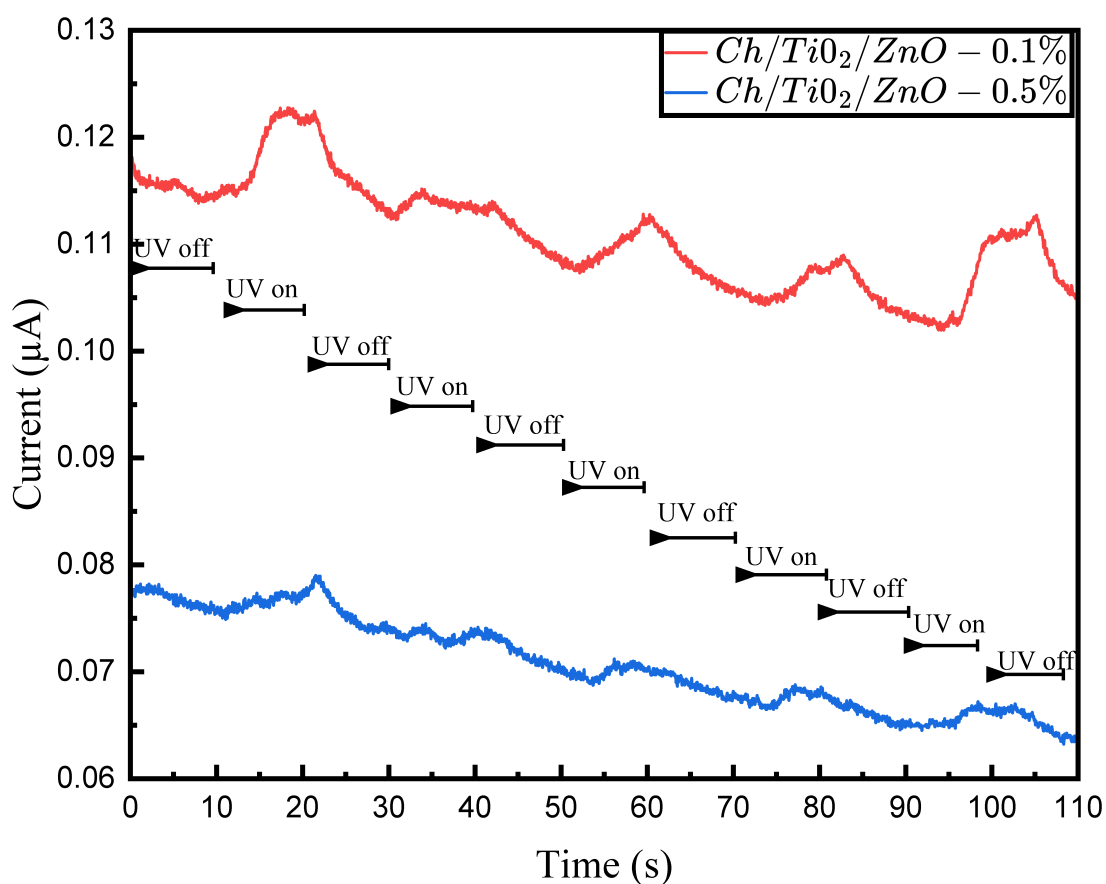


Figure 4.22: Rise and fall curves of Ch/TiO₂/ZnO depending on exposure to UV light(0.1 and 0.5).

Films with a 0.1% concentration of Ch/TiO₂/ZnO exhibit a decrease in current upon UV illumination. This unusual behavior suggests a negative photoconductivity or a light-enhanced charge carrier recombination process.

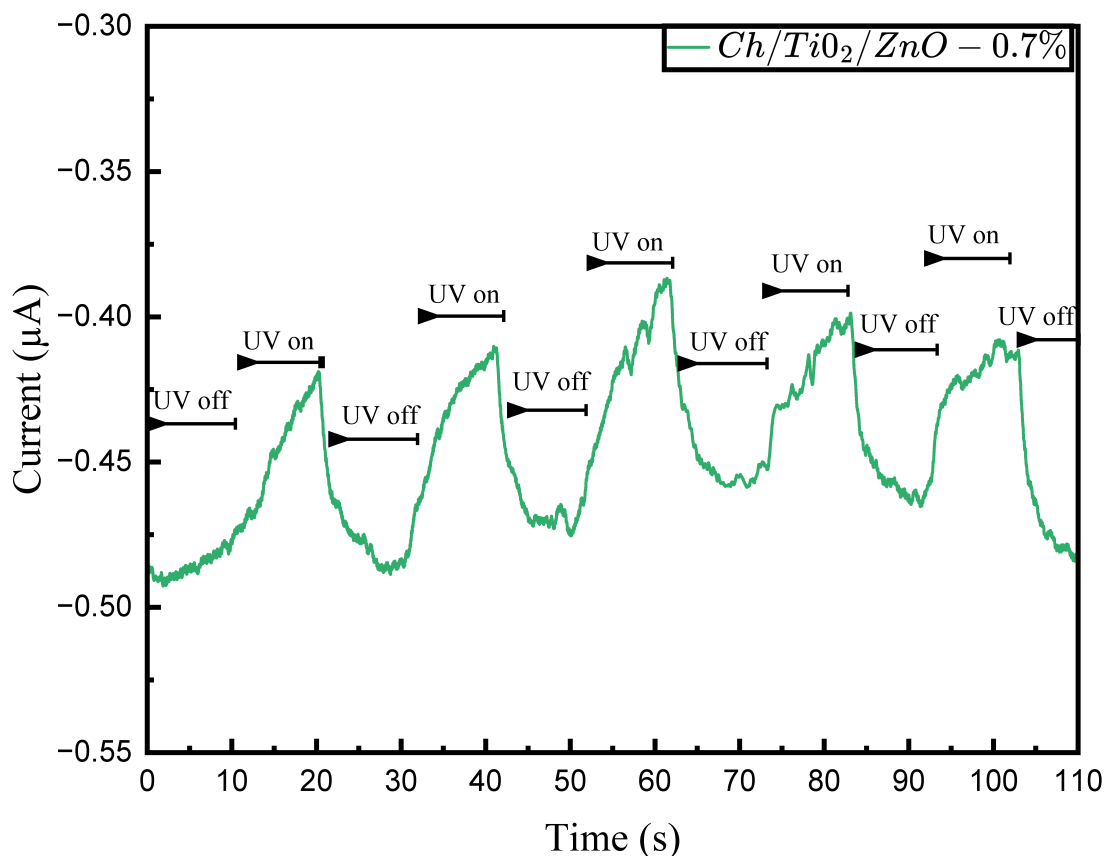


Figure 4.23: Rise and fall curves of Ch/TiO₂/ZnO 0.7% depending on exposure to UV light.

In contrast, films with 0.5% concentration do not show significant changes in current under UV light, indicating a saturation point where additional light does not further increase charge carriers.

The response of the films with 0.5% and 0.7% Ch/TiO₂/ZnO is particularly interesting. The 0.5% concentration in Figure 4.22 maintains a stable current under UV exposure, while the 0.7% concentration in Figure 4.23 shows a notable increase in current. As the concentration of nanoparticles increases, the characteristic photoconductivity properties of TiO₂ begin to prevail. Particularly in the composite film with and 0.7%, there is a noticeable shift towards an increase in photocurrent with UV exposure, which is more aligned with the typical behavior of TiO₂. This observation suggests that at higher concentrations, the TiO₂ component dominates the photoresponse, possibly due to a more continuous network of TiO₂ that facilitates charge transport.

4.13 General Discussion

As a general discussion, we can say that the incorporation of TiO₂ and ZnO nanoparticles in a chitosan matrix has a significant effect on the photoconductive properties of the composite material. XRD analysis confirmed the presence of anatase and wurtzite crystal structures for TiO₂ and ZnO, respectively, indicating that the synthesis conditions maintained the desired crystalline phases of both semiconductors. In addition, UV-Vis and band gap analyses using Tauc's method showed that ZnO and TiO₂ nanoparticles have suitable potential for UV light absorption. This is a relevant finding for applying these materials in UV light sensing. The coating and drying process of the films formed on the interdigitated substrates was crucial to obtain uniform conductivity. It was found that TiO₂ films tend to be more susceptible to damage if recommended drying times are exceeded, which is an important aspect to consider for scale-up device fabrication. There were notable differences in the particle sizes estimated by DLS, which showed larger than expected particle sizes, which could indicate agglomeration in the dispersion or the presence of larger structures in the chitosan matrix. The characterization was improved with another one, which is the AFM, giving us valuable and much clearer information to know the size of the nanoparticles dispersed in the chitosan matrix, being these very promising in terms of dispersion and size achieved.

During the photoconductance tests, the response of the composites under UV illumination showed a clear dependence on composition. It was observed that the presence of chitosan influences the dispersion and stabilization of nanoparticles within the matrix, which may alter the charge transport pathways and affect the overall response to the light stimulus.

Chapter 5

Conclusions & Outlook

The synthesis method adopted in this study allowed us to obtain smaller-size nanoparticles, which is advantageous to increasing the surface area and enhancing the quantum confinement effects. These ZnO and TiO₂ nanoparticles gave us very good results both in UV spectroscopy to get the Band Gap according to the expected elements and properties, also XRD gave us important information of the particle size and purity of them. However, the results of dynamic light scattering suggest a propensity to agglomeration not being the best characterization for this type of film that requires further optimization of the synthesis and dispersion techniques; that is why the observation supported by AFM gave us a better view of the size and dispersion of nanoparticles being this very optimal and useful for the study conducted.

This research has successfully characterized the photoconductive properties of TiO₂ and ZnO nanoparticles within a chitosan matrix. The custom-designed low photoconductance measurement system has been instrumental in quantifying the semiconducting properties of the composite films, revealing the influence of nanoparticle concentration on the photoconductive response. The differing photoresponses of Ch/TiO₂ films offer valuable insights for tailoring material properties for specific end-uses. For instance, lower TiO₂ concentrations could be leveraged in applications requiring a decrease in conductivity under light exposure, while higher concentrations are promising for energy harvesting applications where increased conductivity is advantageous. The results also show that both TiO₂ and ZnO maintain their crystalline integrity and photoconductive capabilities after integration with the biopolymer, although a decrease in performance is observed in ZnO; this may be due to the deep traps that disperse the charge carriers, and finally, we have Ch/TiO₂/ZnO which is influenced by these two semiconductors. The research presented demonstrates a significant advance in the search for safer and more sustainable alternatives for photoconductive materials used in electronic devices. Through this work, a solid starting point has been established by using UV light to evaluate the photoconductance properties of TiO₂ and ZnO-based composites integrated into a chitosan matrix. While these materials operate in the UV spectrum, the ultimate goal is to displace conventional cadmium sulfide and lead sulfide-based photoresists, which operate in the infrared range and present significant environmental and health concerns. Even so, the higher the concentration, the more outstanding results are observed, obtaining each of these interesting results, which reinforces their potential application in optoelectronic devices.

5.1 Future research

This study lays the groundwork for future research focusing on tuning the spectral response more closely to other compounds, such as Copper(II) oxide and Copper(I) oxide compounds with longer wavelengths, approaching the infrared range. Achieving this goal could result in safer and more environmentally friendly alternatives to current photoresists, aligning with a global trend toward green electronics. While this is only the beginning, the results are promising and mark a clear path toward developing more environmentally friendly optoelectronic technologies. There is also ample scope for the practical application of the composites in fabricating photodetectors and solar cells. Testing with real devices will be critical to understanding the performance of the compounds under operational conditions. Moreover, the durability of the photoconductive properties over time and under various environmental conditions remains to be evaluated. These studies will determine the suitability of these materials for long-term application in electronics. Although chitosan is known for its biocompatibility, comprehensive studies on the environmental impact and biodegradability of the composite materials should also be carried out to confirm their environmental friendliness for health and safety applications.

The environmental perspective of this work is underscored by the potential replacement of toxic cadmium- and lead-based photoresistors with these chitosan-based compounds. These findings contribute to not only the reduction of hazardous waste but also open avenues for the development of green electronics.

Appendix A

Crystal size Calculation

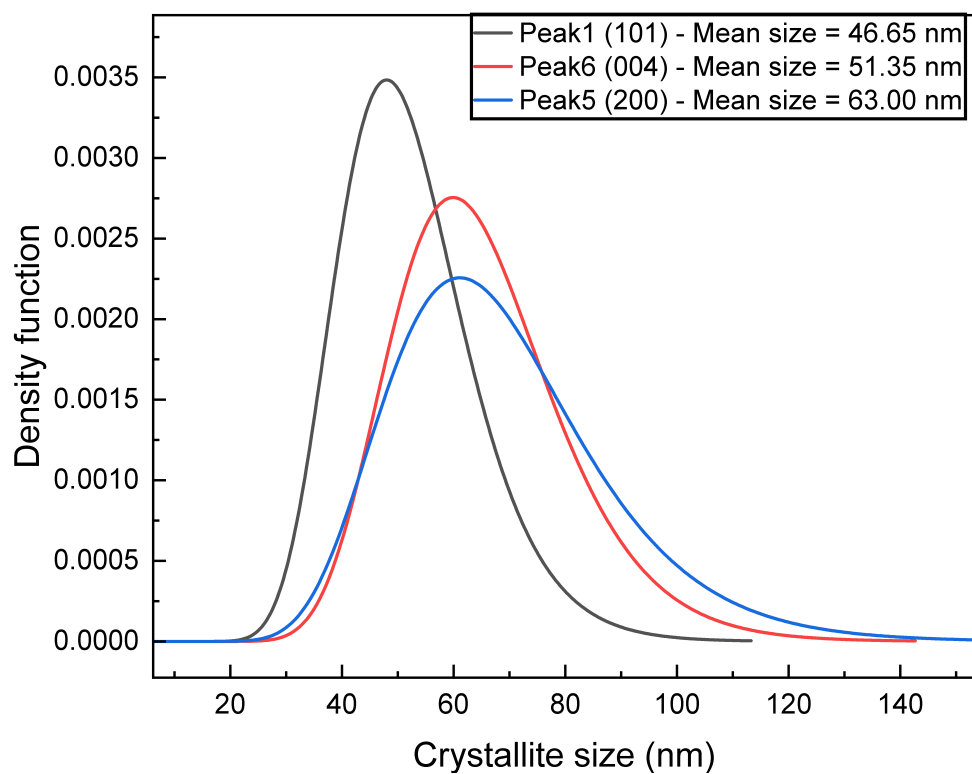


Figure A.1: Mean size of TiO₂ nanoparticles with XRD data using the fundamental parameters of the equipment software at each of the highest peaks.

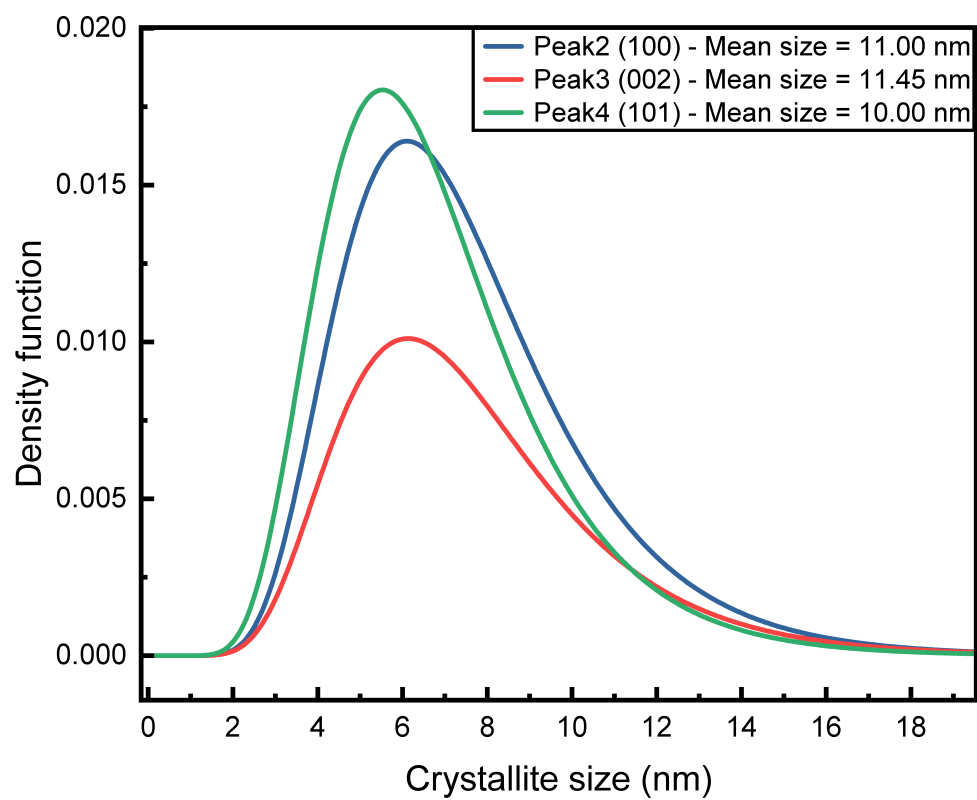


Figure A.2: Mean size of ZnO nanoparticles with XRD data using the fundamental parameters of the equipment software at each of the highest peaks.

Bibliography

- [1] Bangal, M.; Ashtaputer, S.; Marathe, S.; Ethiraj, A.; Hebalkar, N.; Gosavi, S.; Urban, J.; Kulkarni, S. Semiconductor nanoparticles. 2005.
- [2] Hossain, N.; Mobarak, M. H.; Mimona, M. A.; Islam, M. A.; Hossain, A.; Zohur, F. T.; Chowdhury, M. A. Advances and significances of nanoparticles in semiconductor applications—A review. *Results in Engineering* **2023**, 101347.
- [3] Surus, R.; Strzałkowski, K.; Tarczewski, T. High-performance temperature control system for resistance furnace annealing and crystal growth of semiconductor compounds. *Results in Engineering* **2023**, 17, 100863.
- [4] others., *et al.* Review on the processing and properties of polymer nanocomposites and nanocoatings and their applications in the packaging, automotive and solar energy fields. *Nanomaterials* **2017**, 7, 74.
- [5] Miyazaki, T.; Ishikawa, K.; Shirosaki, Y.; Ohtsuki, C. Organic–inorganic composites designed for biomedical applications. *Biological and Pharmaceutical Bulletin* **2013**, 36, 1670–1675.
- [6] Vittal, R.; Ho, K.-C. Zinc oxide based dye-sensitized solar cells: A review. *Renewable and Sustainable energy reviews* **2017**, 70, 920–935.
- [7] Kusdianto, K.; Nugraha, D.; Sekarnusa, A.; Madhania, S.; Machmudah, S.; Winardi, S. ZnO-TiO₂ nanocomposite materials: fabrication and its applications. 2021.
- [8] Adnan, M. A. M.; PHOON, B. L.; Julkapli, N. M. Mitigation of pollutants by chitosan/metallic oxide photocatalyst: a review. *Journal of Cleaner Production* **2020**, 261, 121190.
- [9] Yacobi, B. G. *Semiconductor materials: an introduction to basic principles*; Springer Science & Business Media, 2003.
- [10] Jiang, H.; Hu, P.; Ye, J.; Li, Y.; Li, H.; Zhang, X.; Li, R.; Dong, H.; Hu, W.; Kloc, C. Molecular Crystal Engineering: Tuning Organic Semiconductor from p-type to n-type by Adjusting Their Substitutional Symmetry. *Advanced Materials (Deerfield Beach, Fla.)* **2017**, 29.

- [11] Terna, A. D.; Elemike, E. E.; Mbonu, J. I.; Osafire, O. E.; Ezeani, R. O. The future of semiconductors nanoparticles: Synthesis, properties and applications. *Materials Science and Engineering: B* **2021**, *272*, 115363.
- [12] Abate, A.; Hollman, D. J.; Teuscher, J.; Pathak, S.; Avolio, R.; D'Errico, G.; Vitiello, G.; Fantacci, S.; Snaith, H. J. Protic ionic liquids as p-dopant for organic hole transporting materials and their application in high efficiency hybrid solar cells. *Journal of the american chemical society* **2013**, *135*, 13538–13548.
- [13] Pingel, P.; Arvind, M.; Kölln, L.; Steyrleuthner, R.; Kraffert, F.; Behrends, J.; Janietz, S.; Neher, D. p-type doping of poly (3-hexylthiophene) with the strong Lewis acid tris (pentafluorophenyl) borane. *Advanced Electronic Materials* **2016**, *2*, 1600204.
- [14] Woods-Robinson, R.; Han, Y.; Zhang, H.; Ablekim, T.; Khan, I.; Persson, K. A.; Zakutayev, A. Wide band gap chalcogenide semiconductors. *Chemical reviews* **2020**, *120*, 4007–4055.
- [15] Yan, Y.; Warren, S. C.; Fuller, P.; Grzybowski, B. A. Chemoelectronic circuits based on metal nanoparticles. *Nature Nanotechnology* **2016**, *11*, 603–608.
- [16] Sherly, E. D.; Vijaya, J. J.; Kennedy, L. J.; Meenakshisundaram, A.; Lavanya, M. A comparative study of the effects of CuO, NiO, ZrO₂ and CeO₂ coupling on the photocatalytic activity and characteristics of ZnO. *Korean Journal of Chemical Engineering* **2016**, *33*, 1431–1440.
- [17] others,, *et al.* Synthesis of metal oxide nanoparticles by rapid, high-temperature 3D microwave heating. *Advanced Functional Materials* **2019**, *29*, 1904282.
- [18] Ali, A.; Zafar, H.; Zia, M.; ul Haq, I.; Phull, A. R.; Ali, J. S.; Hussain, A. Synthesis, characterization, applications, and challenges of iron oxide nanoparticles. *Nanotechnology, science and applications* **2016**, 49–67.
- [19] Deng, H.; Qin, C.; Pei, K.; Wu, G.; Wang, M.; Ni, H.; Ye, P. TiO₂/reduced hydroxylated graphene nanocomposite photocatalysts: Improved electron–hole separation and migration. *Materials Chemistry and Physics* **2021**, *270*, 124796.
- [20] Khairy, M.; Zakaria, W. Effect of metal-doping of TiO₂ nanoparticles on their photocatalytic activities toward removal of organic dyes. *Egyptian Journal of Petroleum* **2014**, *23*, 419–426.
- [21] Baskoutas, S. Zinc oxide nanostructures: synthesis and characterization. 2018.
- [22] Giannouli, M.; Govatsi, K.; Syrokostas, G.; Yannopoulos, S. N.; Leftheriotis, G. Factors affecting the power conversion efficiency in ZnO DSSCs: Nanowire vs. nanoparticles. *Materials* **2018**, *11*, 411.
- [23] Xia, C.; Qiao, Z.; Feng, C.; Kim, J.-S.; Wang, B.; Zhu, B. Study on zinc oxide-based electrolytes in low-temperature solid oxide fuel cells. *Materials* **2017**, *11*, 40.

- [24] Joseph, S. M.; Krishnamoorthy, S.; Paranthaman, R.; Moses, J.; Anandharamakrishnan, C. A review on source-specific chemistry, functionality, and applications of chitin and chitosan. *Carbohydrate Polymer Technologies and Applications* **2021**, *2*, 100036.
- [25] Crognale, S.; Russo, C.; Petruccioli, M.; D'annibale, A. Chitosan production by fungi: current state of knowledge, future opportunities and constraints. *Fermentation* **2022**, *8*, 76.
- [26] Pellis, A.; Guebitz, G. M.; Nyanhongo, G. S. Chitosan: Sources, processing and modification techniques. *Gels* **2022**, *8*, 393.
- [27] Omar, B. A.; Elmasry, R.; Eita, A.; Soliman, M. M.; El-Tahan, A. M.; Sitohy, M. Upgrading the preparation of high-quality chitosan from *Procambarus clarkii* wastes over the traditional isolation of shrimp chitosan. *Saudi Journal of Biological Sciences* **2022**, *29*, 911–919.
- [28] Chen, Q.; Qi, Y.; Jiang, Y.; Quan, W.; Luo, H.; Wu, K.; Li, S.; Ouyang, Q. Progress in research of chitosan chemical modification technologies and their applications. *Marine Drugs* **2022**, *20*, 536.
- [29] Sahariah, P.; Másson, M. Antimicrobial chitosan and chitosan derivatives: A review of the structure–activity relationship. *Biomacromolecules* **2017**, *18*, 3846–3868.
- [30] Wang, Q. Z.; Chen, X. G.; Liu, N.; Wang, S. X.; Liu, C. S.; Meng, X. H.; Liu, C. G. Protonation constants of chitosan with different molecular weight and degree of deacetylation. *Carbohydrate polymers* **2006**, *65*, 194–201.
- [31] Wang, W.; Xue, C.; Mao, X. Chitosan: Structural modification, biological activity and application. *International Journal of Biological Macromolecules* **2020**, *164*, 4532–4546.
- [32] Domard, A.; Rinaudo, M. Preparation and characterization of fully deacetylated chitosan. *International Journal of Biological Macromolecules* **1983**, *5*, 49–52.
- [33] Philibert, T.; Lee, B. H.; Fabien, N. Current status and new perspectives on chitin and chitosan as functional biopolymers. *Applied biochemistry and biotechnology* **2017**, *181*, 1314–1337.
- [34] Daraghme, N.; Chowdhry, B. Z.; Leharne, S. A.; Al Omari, M. M.; Badwan, A. A. Co-processed chitin-mannitol as a new excipient for oro-dispersible tablets. *Marine drugs* **2015**, *13*, 1739–1764.
- [35] Dhillon, G. S.; Kaur, S.; Brar, S. K.; Verma, M. Green synthesis approach: extraction of chitosan from fungus mycelia. *Critical reviews in biotechnology* **2013**, *33*, 379–403.
- [36] Casadidio, C.; Peregrina, D. V.; Gigliobianco, M. R.; Deng, S.; Censi, R.; Di Martino, P. Chitin and chitosans: Characteristics, eco-friendly processes, and applications in cosmetic science. *Marine drugs* **2019**, *17*, 369.
- [37] Morin-Crini, N.; Lichtfouse, E.; Torri, G.; Crini, G. Applications of chitosan in food, pharmaceuticals, medicine, cosmetics, agriculture, textiles, pulp and paper, biotechnology, and environmental chemistry. *Environmental Chemistry Letters* **2019**, *17*, 1667–1692.

- [38] Vázquez, J. A.; Rodríguez-Amado, I.; Montemayor, M. I.; Fraguas, J.; del Pilar González, M.; Murado, M. A. Chondroitin sulfate, hyaluronic acid and chitin/chitosan production using marine waste sources: Characteristics, applications and eco-friendly processes: A review. *Marine drugs* **2013**, *11*, 747–774.
- [39] Zainol Abidin, N. A.; Kormin, F.; Zainol Abidin, N. A.; Mohamed Anuar, N. A. F.; Abu Bakar, M. F. The potential of insects as alternative sources of chitin: An overview on the chemical method of extraction from various sources. *International Journal of Molecular Sciences* **2020**, *21*, 4978.
- [40] Anaya-Esparza, L. M.; Ruvalcaba-Gómez, J. M.; Maytorena-Verdugo, C. I.; González-Silva, N.; Romero-Toledo, R.; Aguilera-Aguirre, S.; Pérez-Larios, A.; Montalvo-González, E. Chitosan-TiO₂: A versatile hybrid composite. *Materials* **2020**, *13*, 811.
- [41] Ambegaokar, V.; Halperin, B.; Langer, J. Hopping conductivity in disordered systems. *Physical review B* **1971**, *4*, 2612.
- [42] Murawski, L.; Chung, C.; Mackenzie, J. Electrical properties of semiconducting oxide glasses. *Journal of non-crystalline solids* **1979**, *32*, 91–104.
- [43] Jördens, R.; Strohmaier, N.; Günter, K.; Moritz, H.; Esslinger, T. A Mott insulator of fermionic atoms in an optical lattice. *Nature* **2008**, *455*, 204–207.
- [44] Mazza, G.; Amaricci, A.; Capone, M.; Fabrizio, M. Field-driven Mott gap collapse and resistive switch in correlated insulators. *Physical review letters* **2016**, *117*, 176401.
- [45] Buşilă, M.; Muşat, V.; Textor, T.; Mahltig, B. Synthesis and characterization of antimicrobial textile finishing based on Ag: ZnO nanoparticles/chitosan biocomposites. *Rsc Advances* **2015**, *5*, 21562–21571.
- [46] Tachikawa, T.; Majima, T. Single-molecule, single-particle fluorescence imaging of TiO₂-based photocatalytic reactions. *Chemical Society Reviews* **2010**, *39*, 4802–4819.
- [47] Guo, N.; DiBenedetto, S. A.; Tewari, P.; Lanagan, M. T.; Ratner, M. A.; Marks, T. J. Nanoparticle, size, shape, and interfacial effects on leakage current density, permittivity, and breakdown strength of metal oxide-polyolefin nanocomposites: experiment and theory. *Chemistry of Materials* **2010**, *22*, 1567–1578.
- [48] Prokhorov, E.; Luna-Bárceñas, G.; Yáñez Limón, J. M.; Gómez Sánchez, A.; Kovalenko, Y. Chitosan-ZnO nanocomposites assessed by dielectric, mechanical, and piezoelectric properties. *Polymers* **2020**, *12*, 1991.
- [49] Siripatrawan, U.; Kaewklin, P. Fabrication and characterization of chitosan-titanium dioxide nanocomposite film as ethylene scavenging and antimicrobial active food packaging. *Food Hydrocolloids* **2018**, *84*, 125–134.
- [50] Xiao, G.; Zhang, X.; Zhao, Y.; Su, H.; Tan, T. The behavior of active bactericidal and antifungal coating under visible light irradiation. *Applied surface science* **2014**, *292*, 756–763.
- [51] Nithya, A.; Jothivenkatachalam, K. Visible light assisted TiO₂-chitosan composite for removal of reactive dye. *J. Environ. Nanotechnol* **2014**, *3*, 20–26.

- [52] Lin, B.; Luo, Y.; Teng, Z.; Zhang, B.; Zhou, B.; Wang, Q. Development of silver/titanium dioxide/chitosan adipate nanocomposite as an antibacterial coating for fruit storage. *LWT-Food Science and Technology* **2015**, *63*, 1206–1213.
- [53] Saad, A. M.; Abukhadra, M. R.; Ahmed, S. A.-K.; Elzanaty, A. M.; Mady, A. H.; Betiha, M. A.; Shim, J.-J.; Rabie, A. M. Photocatalytic degradation of malachite green dye using chitosan supported ZnO and Ce–ZnO nano-flowers under visible light. *Journal of environmental management* **2020**, *258*, 110043.
- [54] Haldorai, Y.; Shim, J.-J. Chitosan-zinc oxide hybrid composite for enhanced dye degradation and antibacterial activity. *Composite Interfaces* **2013**, *20*, 365–377.
- [55] Krishnaveni, R.; Thambidurai, S. Industrial method of cotton fabric finishing with chitosan–ZnO composite for anti-bacterial and thermal stability. *Industrial Crops and Products* **2013**, *47*, 160–167.
- [56] Duong, N. T.; Vuong, L. D.; Son, N. M.; Van Tuyen, H.; Van Chuong, T. The synthesis of TiO₂ nanoparticles using sulfuric acid method with the aid of ultrasound. *Nanomaterials and Energy* **2017**, *6*, 82–88.
- [57] Wang, X.; Sun, T.; Yang, J.; Zhao, L.; Jia, J. Low-temperature H₂S removal from gas streams with SBA-15 supported ZnO nanoparticles. *Chemical Engineering Journal* **2008**, *142*, 48–55.
- [58] Özgür, Ü.; Alivov, Y. I.; Liu, C.; Teke, A.; Reshchikov, M. A.; Doğan, S.; Avrutin, V.; Cho, S.-J.; Morkoç, H. A comprehensive review of ZnO materials and devices. *Journal of applied physics* **2005**, *98*.
- [59] Linsebigler, A. L.; Lu, G.; Yates Jr, J. T. Photocatalysis on TiO₂ surfaces: principles, mechanisms, and selected results. *Chemical reviews* **1995**, *95*, 735–758.
- [60] Bouazizi, N.; Ajala, F.; Khelil, M.; Lachheb, H.; Khirouni, K.; Houas, A.; Azzouz, A. Zinc oxide incorporating iron nanoparticles with improved conductance and capacitance properties. *Journal of Materials Science: Materials in Electronics* **2016**, *27*, 11168–11175.
- [61] Kim, M.; Bae, C.; Kim, H.; Yoo, H.; Moreno, J. M. M.; Jung, H. S.; Bachmann, J.; Nielsch, K.; Shin, H. Confined crystallization of anatase TiO₂ nanotubes and their implications on transport properties. *Journal of Materials Chemistry A* **2013**, *1*, 14080–14088.
- [62] Franco, A.; Pessoni, H. Enhanced dielectric constant of Co-doped ZnO nanoparticulate powders. *Physica B: Condensed Matter* **2015**, *476*, 12–18.
- [63] Manikandan, A.; Vijaya, J.; Ragupathi, C.; Kennedy, L. J. Optical properties and dye-sensitized solar cell applications of ZnO nanostructures prepared by microwave combustion synthesis. *Journal of Nanoscience and Nanotechnology* **2014**, *14* 3, 2584–2590.
- [64] Jain, P. K.; Lee, K. S.; El-Sayed, I. H.; El-Sayed, M. A. Calculated absorption and scattering properties of gold nanoparticles of different size, shape, and composition: applications in biological imaging and biomedicine. *The journal of physical chemistry B* **2006**, *110*, 7238–7248.

- [65] Evanoff, D. D.; Chumanov, G. Size-controlled synthesis of nanoparticles. 2. Measurement of extinction, scattering, and absorption cross sections. *The Journal of Physical Chemistry B* **2004**, *108*, 13957–13962.
- [66] Chen, S.; Guo, Y.; Chen, S.; Yu, H.; Ge, Z.; Zhang, X.; Zhang, P.; Tang, J. Facile preparation and synergistic antibacterial effect of three-component Cu/TiO₂/CS nanoparticles. *Journal of Materials Chemistry* **2012**, *22*, 9092–9099.
- [67] Adak, B.; Butola, B.; Joshi, M. Calcination of UV shielding nanopowder and its effect on weather resistance property of polyurethane nanocomposite films. *Journal of Materials Science* **2019**, *54*, 12698–12712.
- [68] others., *et al.* Synthesis of ZnO-TiO₂/Chitosan nanorods by using precipitation methods and studying their structures and optics properties at different precursor molar compositions. 2019.
- [69] Zhu, H.; Jiang, R.; Fu, Y.; Guan, Y.; Yao, J.; Xiao, L.; Zeng, G. Effective photocatalytic decolorization of methyl orange utilizing TiO₂/ZnO/chitosan nanocomposite films under simulated solar irradiation. *Desalination* **2012**, *286*, 41–48.
- [70] Mondelaers, D.; Vanhoyland, G.; Van den Rul, H.; D'haen, J.; Van Bael, M.; Mullens, J.; Van Poucke, L. Synthesis of ZnO nanopowder via an aqueous acetate–citrate gelation method. *Materials research bulletin* **2002**, *37*, 901–914.
- [71] Marchand, A. P.; Reddy, G. M. Mild and Highly Selective Ultrasound-Promoted Zinc/Acetic Acid Reduction of C=C Bonds in α, β -Unsaturated γ -Dicarbonyl Compounds. *Synthesis* **1991**, *1991*, 198–200.
- [72] Petrozza, A.; Groves, C.; Snaith, H. J. Electron transport and recombination in dye-sensitized mesoporous TiO₂ probed by photoinduced charge-conductivity modulation spectroscopy with Monte Carlo modeling. *Journal of the American Chemical Society* **2008**, *130*, 12912–12920.
- [73] Furube, A.; Tamaki, Y.; Murai, M.; Hara, K.; Katoh, R.; Tachiya, M. Femtosecond visible-to-IR spectroscopy of TiO₂ nanocrystalline films: Dynamics of UV-generated charge carrier relaxation at different excitation wavelengths. 2007.
- [74] George, S.; Pokhrel, S.; Ji, Z.; Henderson, B. L.; Xia, T.; Li, L.; Zink, J. I.; Nel, A. E.; Madler, L. Role of Fe doping in tuning the band gap of TiO₂ for the photo-oxidation-induced cytotoxicity paradigm. *Journal of the American Chemical Society* **2011**, *133*, 11270–11278.
- [75] Sahimi, M. *Applications of percolation theory*; CRC Press, 1994.
- [76] Lanje, A. S.; Sharma, S. J.; Ningthoujam, R. S.; Ahn, J.-S.; Pode, R. B. Low temperature dielectric studies of zinc oxide (ZnO) nanoparticles prepared by precipitation method. *Advanced Powder Technology* **2013**, *24*, 331–335.
- [77] Yu, G.; Cheng, Y.; Duan, Z. Study of the electrical conductivity characteristics of micro and nano-ZnO/LDPE composites. *Molecules* **2022**, *27*, 3674.